CM² MAGAZINE

第 41 期

南方科技大学海洋磁学中心主编

创刊词

海洋是生命的摇篮，是文明的纽带。地球上最早的生命诞生于海洋，海洋里的生命最终进化成了人类，人类的文化融合又通过海洋得以实现。人因海而兴。

人类对海洋的探索从未停止。从远古时代美丽的神话传说，到麦哲伦的全球航行，再到现代对大洋的科学钻探计划，海洋逐渐从人类敬畏崇拜幻想的精神寄托演变成可以开发利用与科学研究的客观存在。其中，上个世纪与太空探索同步发展的大洋科学钻探计划将人类对海洋的认知推向了崭新的纬度：深海（deep sea）与深时（deep time）。大洋钻探计划让人类知道，奔流不息的大海之下，埋藏的却是亿万年的地球历史。它们记录了地球板块的运动，从而使板块构造学说得到证实；它们记录了地球环境的演变，从而让古海洋学方兴未艾。

在探索海洋的悠久历史中，从大航海时代的导航，到大洋钻探计划中不可或缺的磁性地层学，磁学发挥了不可替代的作用。这不是偶然，因为从微观到宏观，磁性是最基本的物理属性之一，可以说，万物皆有磁性。基于课题组的学科背景和对海洋的理解，我们对海洋的探索以磁学为主要手段，海洋磁学中心因此而生。

海洋磁学中心，简称 CM^2，一为其全名“Centre for Marine Magnetism”的缩写，另者恰与爱因斯坦著名的质能方程 $E = MC^2$ 对称，借以表达我们对科学巨匠的敬仰和对科学的不懈追求。

然而科学从来不是单打独斗的产物。我们以磁学为研究海洋的主攻利器，但绝不仅限于磁学。凡与磁学相关的领域均是我们关注的重点。为了跟踪反映国内外地球科学特别是与磁学有关的地球科学领域的最新研究进展，海洋磁学中心特地主办 CM^2 Magazine，以期与各位地球科学工作者相互交流学习、合作共进！

“海洋孕育了生命，联通了世界，促进了发展”。 21 世纪是海洋科学的时代，由陆向海，让我们携手迈进中国海洋科学的黄金时代

目 录

岩石磁学演绎

第 31 章　钛磁铁矿与钛磁赤铁矿

和赤铁矿与针铁矿一样，磁铁矿的晶格中也会掺入杂质，最为常见的是 Ti^{4+}，形成钛磁铁矿 $Fe_{3-x}Ti_xO_4$ (0<x<1)，文献中，钛磁铁矿常简写成 TMx，比如 TM60 表示 $Fe_{2.4}Ti_{0.6}O_4$。

当 X＝0 时，就是磁铁矿（Fe_3O_4），当 X＝1 时，就是钛尖晶石（Fe_2TiO_4）。对于钛尖晶石，其晶格结构中不含有三价铁离子，其价态模式为 $Fe^{2+}(Fe^{2+}Ti^{4+})O_4$。

随着含钛量的增加，钛磁铁矿的性质会显著变化。首先其居里温度会随着含钛量的增加而降低。对于 TM80，其 T_C 就已经低至室温，从而变为顺磁性。对于 TM60，其 T_C 在 150-200 ℃之间，非常容易和铁硫化物弄混。区别在于 TM 系列是热稳定性的，而铁硫化物热不稳定。对于钛尖晶石（Fe_2TiO_4），其 T_C 低于-100 ℃，在室温下也为顺磁性物质。

由于 Ti^{4+}的离子半径比 Fe^{2+}要大，所以随着钛含量的增加，钛磁铁矿的晶格变大，饱和磁化强度降低。同时矫顽力会大幅度增加，这可能是两种机制造成的，一种是增加了磁弹性能，第二种是降低了 M_s。

钛磁铁矿在自然界中还常常被氧化，变成钛磁赤铁矿。

$$Fe^{3+}_{[2-2x+z(1+x)]R}Fe^{2+}_{(1+x)(1-z)R}Ti^{4+}_{xR}\square_{3(1-R)}O^{2-}_4$$

其中 R = 8/[8+z(1+x)]，0≤ z ≤ 1。

钛磁铁矿被氧化后，其分子式变得非常复杂，其中包含两个重要参数 x 和氧化度 z。同时，还产生了一定量的空位。

氧化过程中，先消耗八面体内的 Fe^{2+}，M_B 降低，当 B 区的 Fe^{2+}消耗完，A 区的 Fe^{2+}开始被消耗，M_A 降低。为了达到平衡，在 A 区产生的空位会扩散到 B 区，也就是 B 区的铁离子扩散到 A 区，这叫 ionic ordering。此时，M_B 继续降低，M_A 会有所升高。

没有氧化时，$M_B>M_A$。氧化后，可不可能 $M_B<M_A$?

如果可能，此时获得的 CRM 的方向与外加场什么关系？

显而易见，钛磁铁矿在氧化后，其磁矩有可能变成负的，造成反向磁化的效果。也就是说，当你正向加场时，得到的确实负的剩磁。当钛的含量高于 60 mol%，氧化度高于 0.5 时，就有可能出现反向磁化的现象。

在最早发现岩石能够记录反向磁场方向时，有两种主要的机制：地磁场倒转与磁性矿物反向磁化。随着研究的深入，全球各地，各种介质都记录了负极性，这不可能全用反向磁化来解释，于是慢慢的地磁极性倒转机制被确认，引发了地学的重大革命。

但是，这不等于反向磁化现象不存在。如下图所示，在中温段，剩磁不但不降低，反而会升高，使得退磁特征出现平行的三段特征。这个中等温度段的剩磁代表着反向磁化（Doubrovine and Tarduno, 2006）。

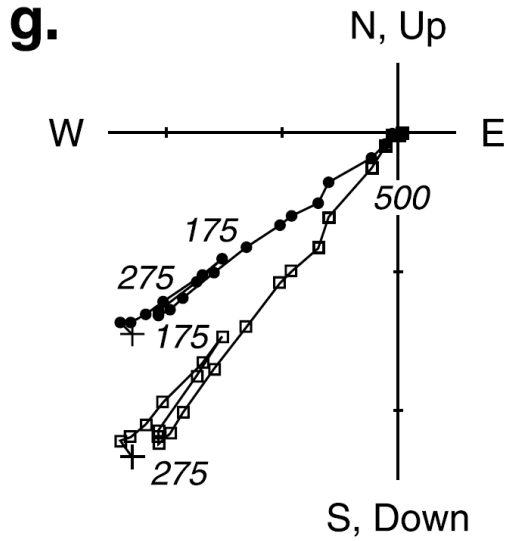

图 1 典型反向磁化的样品热退磁 Z 氏图（Doubrovine and Tarduno, 2006）

钛磁铁矿主要产于岩浆矿床中，在火成岩中分布较为广泛，尤其在大洋玄武岩中，是主要的剩磁携带者。因此，在大洋中观测到的磁异常条带，钛磁铁矿的贡献很大。随着时间变老，钛磁铁矿逐渐氧化，其 Ms 和剩磁会降低，这使海底磁条带记录的磁信号从老到新减弱，造成我们对地磁场演化趋势的误判。在氧化过程中，其居里温度会逐渐上升，造成居里面（Tc：150 ℃→500 ℃）变得更深。

文献速递

1. 晚第四纪以来白令海东部的海冰及沉积氧化还原研究：对北太平洋中层水通风机大西洋-太平洋跷跷板效应的指示

Henrieka Detlef, Sindia M. Sosdian, Simon T. Belt, et al.,* **翻译人：仲义 zhongy@sustech.edu.cn**

Late quaternary sea-ice and sedimentary redox conditions in the eastern Bering Sea – Implications for ventilation of the mid-depth North Pacific and an Atlantic-Pacific seesaw mechanism [J]. Quaternary Science Reviews*, 2020, 106549.* https://doi.org/10.1016/j.quascirev.2020.106549.

摘要：在冰期-间冰期和千年尺度上，海冰是高纬度海洋环流和初级生产力的重要影响因素，其直接驱动区域性和全球生物地球化学循环过程。在现代北太平洋地区，当鄂霍次克海海冰形成时期，盐水大量输入导致北太平洋中层水形成（NPIW），导致在北太平洋 300-1000m 水深地区的通风作用增强。然而，北太平洋中层水的通风作用成因仍然存在争议。数值模拟结果显示北大西洋和北太平洋之间通过大气传输存在较强的遥相关，并响应于北大西洋径向翻转流的减弱和停止。这会导致了北太平洋表层海水盐度的增加，并触发深层通风作用的增强。换句话来说，北太平洋及其边缘海的海冰形成的增强，可能导致深层水翻转作用增强。作者利用白令海东部 U1343 站位基于 40 ka 以来多指标方法调查海冰动态、沉积氧化还原指标和底栖有孔虫的生态变化特征。研究结果显示，Heinrich 1 早期海冰形成扩张会局部性地减弱了盐跃层，有助于触发深层翻转流作用。除此之外，冰川冰消期时期，海冰退缩可能促进初级生产力的提高及该站位中深度缺氧的扩张，证实了海冰在冰消期北太平洋碳循环过程的发挥了重要作用。

ABSTRACT: On glacial-interglacial and millennial timescales, sea ice is an important player in the circulation and primary productivity of high latitude oceans, affecting regional and global biogeochemical cycling. In the modern North Pacific, brine rejection during sea-ice freezing in the Sea of Okhotsk drives the formation of North Pacific Intermediate Water (NPIW) that ventilates the

North Pacific Ocean at 300 me1000 m water depth. Glacial intervals of the late Quaternary, however, experienced a deepening of glacial NPIW to at least 2000 m, with the strongest ventilation observed during cold stadial conditions of the last deglaciation. However, the origin of the shifts in NPIW ventilation is poorly understood. Numerical simulations suggest an atmospheric teleconnection between the North Atlantic and the North Pacific, in response to a slowdown or shutdown of the Atlantic meridional overturning circulation. This leads to a build-up of salinity in the North Pacific surface ocean, triggering deep ventilation. Alternatively, increased sea-ice formation in the North Pacific and its marginal seas may have caused strengthened overturning in response to enhanced brine rejection. Here we use a multi-proxy approach to explore sea-ice dynamics, sedimentary redox chemistry, and benthic ecology at Integrated Ocean Drilling Program Site U1343 in the eastern Bering Sea across the last 40 ka. Our results suggest that brine rejection from enhanced sea-ice formation during early Heinrich Stadial 1 locally weakened the halocline, aiding in the initiation of deep overturning. Additionally, deglacial sea-ice retreat likely contributed to increased primary productivity and expansion of mid-depth hypoxia at Site U1343 during interstadial conditions, confirming a vital role of sea ice in the deglacial North Pacific carbon cycle.

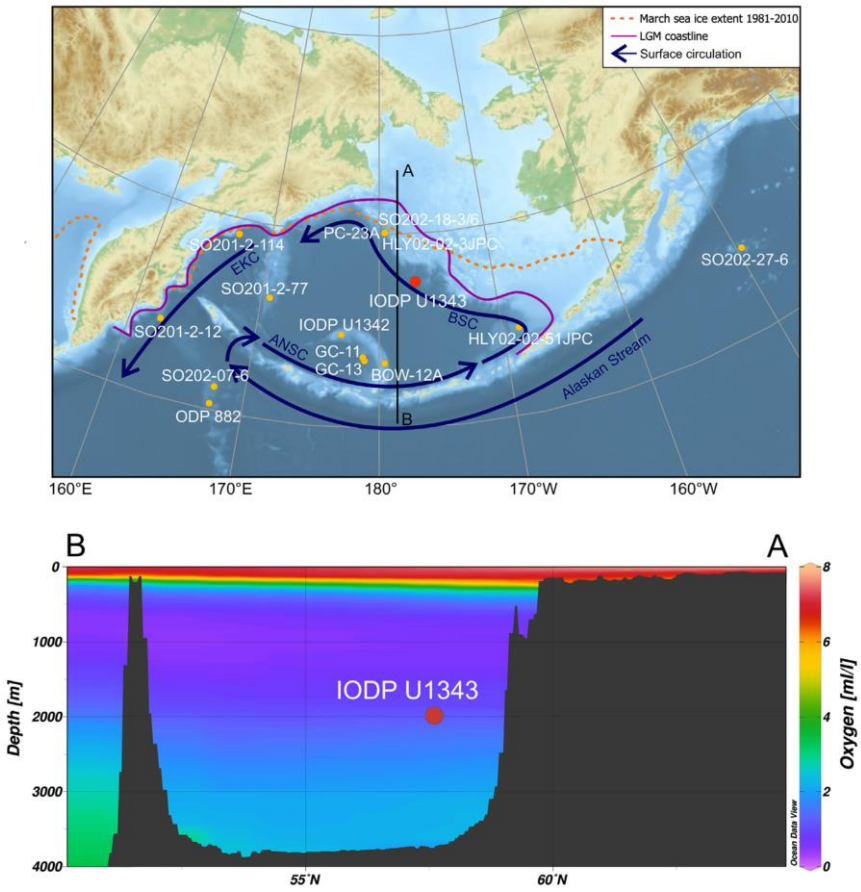

Figure 1. Map of the Bering Sea (top) and annual mean oxygen concentrations (Boyer et al., 2013) along a north (A) south (B) transect in the central Bering Sea (bottom) drawn with Ocean Data View (Schlitzer, 2016) (bathymetry from 'The GEBCO_2014 Grid, version 20,141,103, http://www.gebco.netr'). IODP Site U1343 is indicated with a red dot, additional core locations discussed in the text are marked with yellow dots. The map shows the surface ocean circulation (dark blue), including the Alaskan Stream, the Aleutian North Slope Current (ANSC), the Bering Slope Current (BSC), and the East Kamchatka Current (EKC). The maximum winter sea-ice extent between 1981 and 2010 is indicated as an orange dashed line (Fetterer et al., 2017) and the last glacial maximum (LGM) coastline is shown in purple (The PALE Beringian Working Group, 1999). (For interpretation of the references to color in this figure legend, the reader is referred to the Web version of this article.)

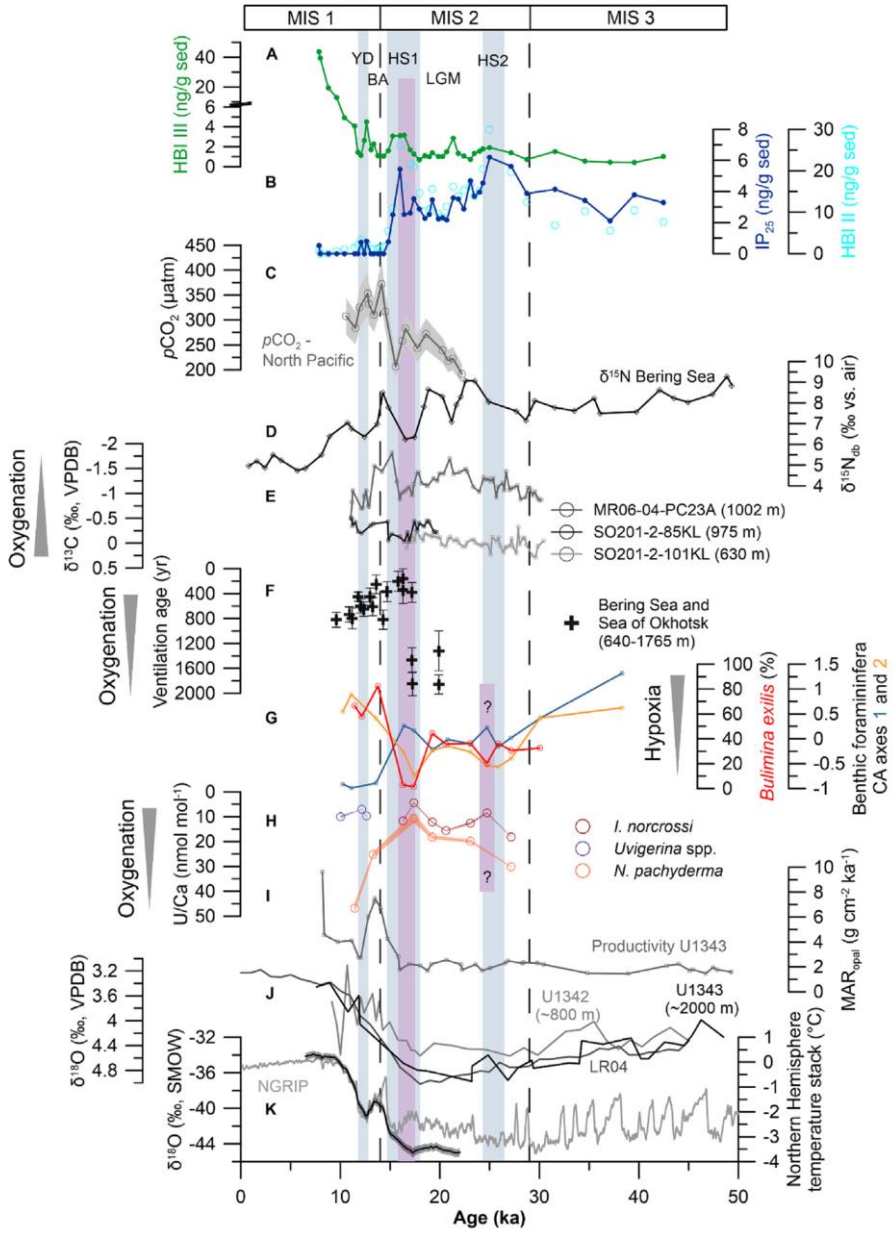

Figure 2. A compilation of ventilation and carbon cycle records discussed in this manuscript in combination with regional and global climate records. (A) HBI III (green) at Site U1343 (this study); (B) IP25 (dark blue) together with HBI II (light blue circles) (this study); (C) North Pacific pCO2 at MD01-2416 (Gray et al., 2018); (D) Diatom-bound d15N at JPC17 (Brunelle et al., 2007); (E) Benthic foraminiferal d13C at MR06-04-PC23A (medium grey) (Rella et al., 2012), SO201-2-85 KL (dark grey), and SO201-2-101 KL (light grey) (Max et al., 2014); (F) Intermediate water ventilation ages in the Bering Sea and the Sea of Okhotsk (Max et al., 2014); (G) Scores of the benthic foraminiferal assemblage correspondence analysis axis 1 (blue) and 2 (yellow) and the relative abundance of the benthic

foraminifera Bulimina exilis (red) at Site U1343; (H) U/Ca of N. pachyderma (orange), I. norcrossi (red), and Uvigerina spp. (purple) at Site U1343; (I) MARopal at Site U1343 (Kim et al., 2014); (J) Benthic foraminiferal d18O at IODP Site U1342 (light grey) (Knudson and Ravelo, 2015), Site U1343 (black) (Asahi et al., 2016), and the LR04 stack (grey) (Lisiecki and Raymo, 2005); (K) NGRIP d18O on the GICC05 time scale (Rasmussen et al., 2006; Svensson et al., 2008; Vinther et al., 2006), and the Northern Hemisphere temperature stack including a 1s error envelope (Shakun et al., 2012). The light blue shaded vertical bars indicate the YD, HS1, and HS2, the pink vertical bars indicate intervals with imrpoved ventilation at Site U1343. (For interpretation of the references to color in this figure legend, the reader is referred to the Web version of this article.)

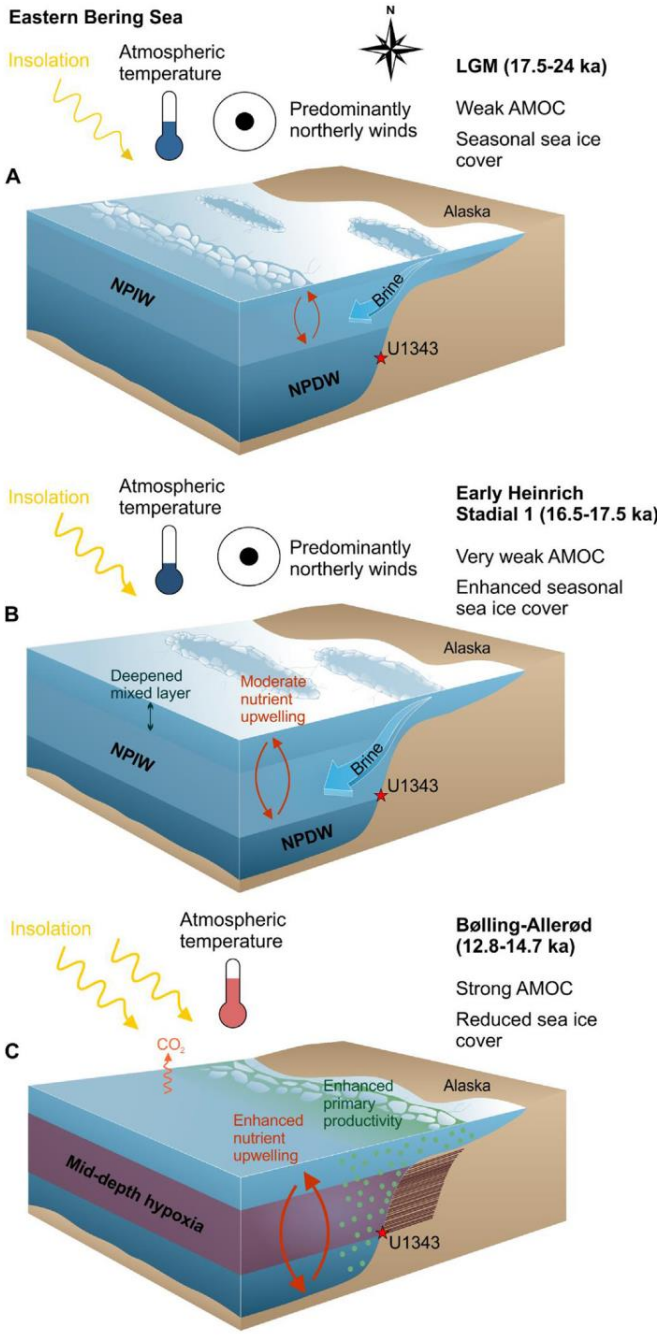

Figure 3. Simplified schematic of the deglacial sea-ice dynamics, intermediate water ventilation, and biogeochemical cycling in the eastern Bering Sea. The schematic was produced using features from the IAN symbol library (Courtesy of the Integration and Application Network, University of Maryland Center for Environmental Science (ian.umces.edu/symbols/)). (A) The LGM (17.5~24 ka) was characterized by a seasonal sea-cover, reduced upwelling of NPDW, and an expanded GNPIW resulting from enhanced brine rejection. GNPIW, however, did not reach to depth of 2000 m. (B) Early HS1 (16.5~17.5 ka) was characterized by an enhanced seasonal sea-ice cover, in response to atmospheric

cooling. Increased sea-ice formation led to enhanced brine rejection and increased GNPIW formation and ventilation compared to the LGM, which in turn caused modest up-mixing of nutrients, as well as a deepening of the mixed layer resulting in light limitation of primary producers. (C) The B-A (12.8~14.7 ka) is marked by a reduced sea-ice cover due to atmospheric warming, enhanced NPDW upwelling, increased primary productivity, and pronounced mid-depth hypoxia causing the preservation of laminations along the eastern Bering Sea slope.

2. 超深部钻石记录了岩石圈到上地幔的碳循环

翻译人：蒋晓东 jiangxd@sustech.edu.cn

Regier M E, Pearson D G, Stachel T, et al. ***The lithospheric-to-lower-mantle carbon cycle recorded in superdeep diamonds [J]. Nature****, 2020, 585, 234-239.*

https://doi.org/10.1038/s41586-020-2676-z

摘要：碳从地球表面传输到地幔是地球碳循环的重要环节，这影响了气候以及表层地球和地幔的氧化还原态。在这个循环中最大的不确定性是碳到达地幔的深度，即海洋沉积物和蚀变洋壳中的碳进入深部及对地幔碳的贡献。下部岩石圈的包裹体或者深部钻石（来自超 250 公里深）可用于限定这些变化。本研究对取自几内亚坎坎的深度到达上地幔（超过 660 公里）的钻石进行包裹体的氧同位素测试。这些数据与钻石的碳、氮同位素分析表明碳化的火山岩洋壳而非沉积物是版块俯冲到深部转换带的碳源。在这样的深度内，下部岩石圈包裹体相对于来自地球的榴辉岩圈的包裹体更富集 ^{18}O。下地壳中增长的 ^{18}O 量是由于富碳俯冲岩石圈熔融重结晶。相反，下地幔包裹体以及相应钻石具有较小变化范围的同位素值，这是典型的地幔特征而无地壳作用。在缩小的贫挥发分的下地幔中碳储存在矿物中而非钻石中，因此碳必须活化并且富集。我们的数据支持这个模型，即洋壳岩石圈俯冲下地幔最上部而发生的水合作用使带有金属元素的碳形成钻石，这一过程并未受到周围稳定同位素的影响。从碳酸盐板片熔融到下地幔板片脱水的转变过程支持下地幔对碳俯冲具有屏障作用。

ABSTRACT: The transport of carbon into Earth's mantle is a critical pathway in Earth's carbon cycle, affecting both the climate and the redox conditions of the surface and mantle. The largest unconstrained variables in this cycle are the depths to which carbon in sediments and altered oceanic crust can be subducted and the relative contributions of these reservoirs to the sequestration of carbon in the deep mantle. Mineral inclusions in sublithospheric, or 'superdeep', diamonds (derived from depths greater than 250 kilometres) can be used to constrain these variables. Here we present oxygen isotope measurements of mineral inclusions within diamonds from Kankan, Guinea that are derived from depths extending from the lithosphere to the lower mantle (greater than 660

kilometres). These data, combined with the carbon and nitrogen isotope contents of the diamonds, indicate that carbonated igneous oceanic crust, not sediment, is the primary carbon-bearing reservoir in slabs subducted to deep-lithospheric and transition-zone depths (less than 660 kilometres). Within this depth regime, sublithospheric inclusions are distinctly enriched in ^{18}O relative to eclogitic lithospheric inclusions derived from crustal protoliths. The increased ^{18}O content of these sublithospheric inclusions results from their crystallization from melts of carbonate-rich subducted oceanic crust. In contrast, lower-mantle mineral inclusions and their host diamonds (deeper than 660 kilometres) have a narrow range of isotopic values that are typical of mantle that has experienced little or no crustal interaction. Because carbon is hosted in metals, rather than in diamond, in the reduced, volatile-poor lower mantle, carbon must be mobilized and concentrated to form lower-mantle diamonds. Our data support a model in which the hydration of the uppermost lower mantle by subducted oceanic lithosphere destabilizes carbon-bearing metals to form diamond, without disturbing the ambient-mantle stable-isotope signatures. This transition from carbonate slab melting in the transition zone to slab dehydration in the lower mantle supports a lower-mantle barrier for carbon subduction.

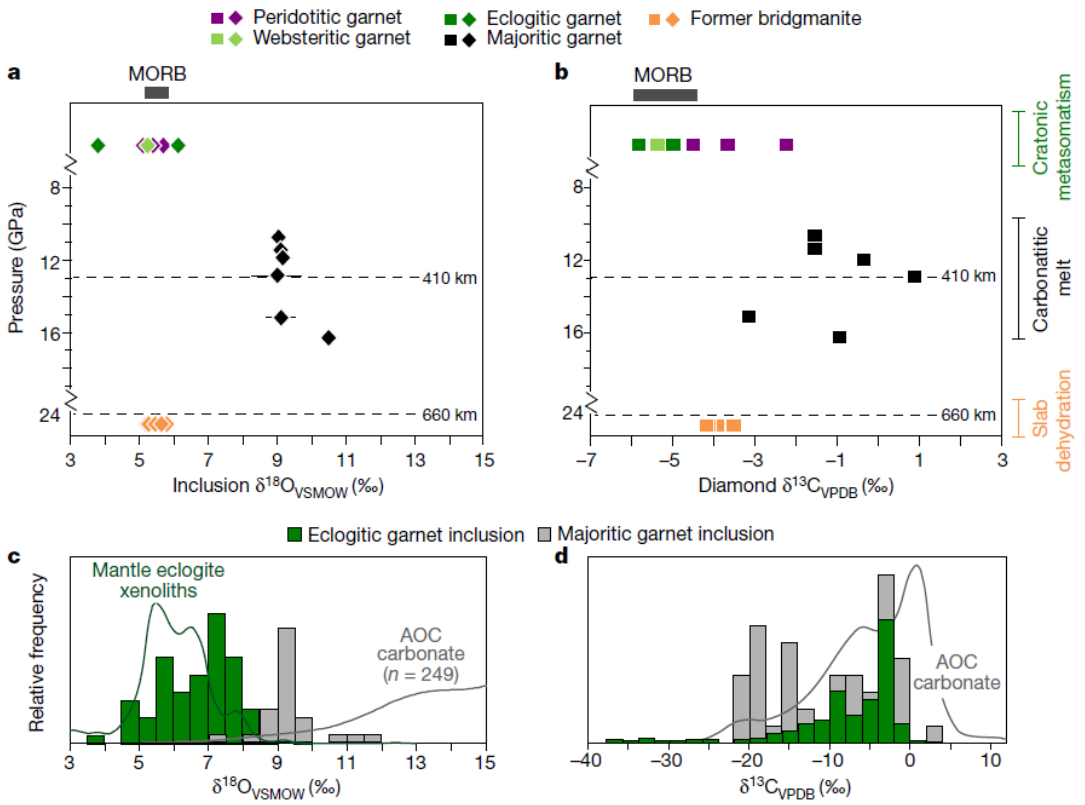

Figure 1. Stable-isotope compositions of diamonds and their mineral inclusions. a, b, Silicate inclusion $\delta^{18}O$ and diamond host $\delta^{13}C$ signatures versus depth for a suite of Kankan diamonds. Errors are 2σ and often smaller than the symbol. MORB isotopic ranges are indicated by grey bars. Inferred environments of formation are indicated on the right. c, A histogram of $\delta^{18}O$ for all measured majoritic garnet inclusions (grey, n = 26) has a more positive mode than that for eclogitic garnet inclusions (green, n = 64). Also plotted are probability density functions of eclogitic garnets from mantle xenoliths (green line; bandwidth of 0.2‰) and AOC carbonates (grey line; bandwidth of 1.9‰). d, Histograms of $\delta^{13}C$ for a worldwide database of eclogitic (green, n = 467) and majoritic garnet-bearing diamonds (grey, n = 48) and a probability density function (bandwidth of 1.17‰) for AOC carbonate. Note that the scale differs from that of Fig. 1b. References for the data shown in this figure are provided in the source data file.

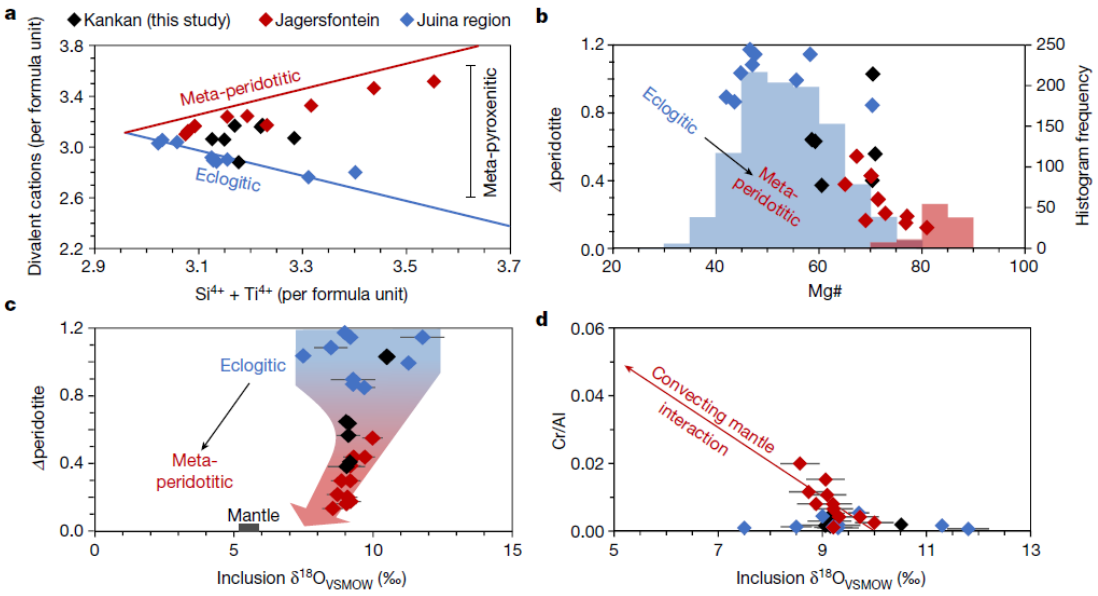

Figure 2. Elemental and isotopic composition of majoritic garnet inclusions. a, Divalent cations (Fetotal, Mg, Ca, Mn) versus Si and Ti per formula unit ([O] = 12) in majoritic garnets from Kankan, Jagersfontein and the Juina region. Red and blue lines show substitutions typical for meta-peridotitic and eclogitic compositions, respectively, which begin at the median value for eclogitic garnets. b, Majoritic garnet Mg# [Mg/(Mg+Fe) × 100] versusΔperidotite, which indicates the deviation of an individual garnet from the meta-peridotitic substitution. The secondary-axis histograms show the distribution of Mg# in lithospheric eclogitic (blue) and peridotitic (red) garnet inclusions. c, $\delta^{18}O$ versus Δperidotite for majoritic garnet. d, Cr/Al and $\delta^{18}O$ in majoritic garnets. The red line is a linear regression (r^2 = 0.6) for

the Jagersfontein data, which trends from low Cr/Al eclogitic majorites to more meta-peridotitic, high-Cr/Al majorites with lower $\delta^{18}O$. Error bars in c, d are 2σ and may be smaller than the symbols. References for the data shown in this figure are provided in the source data file.

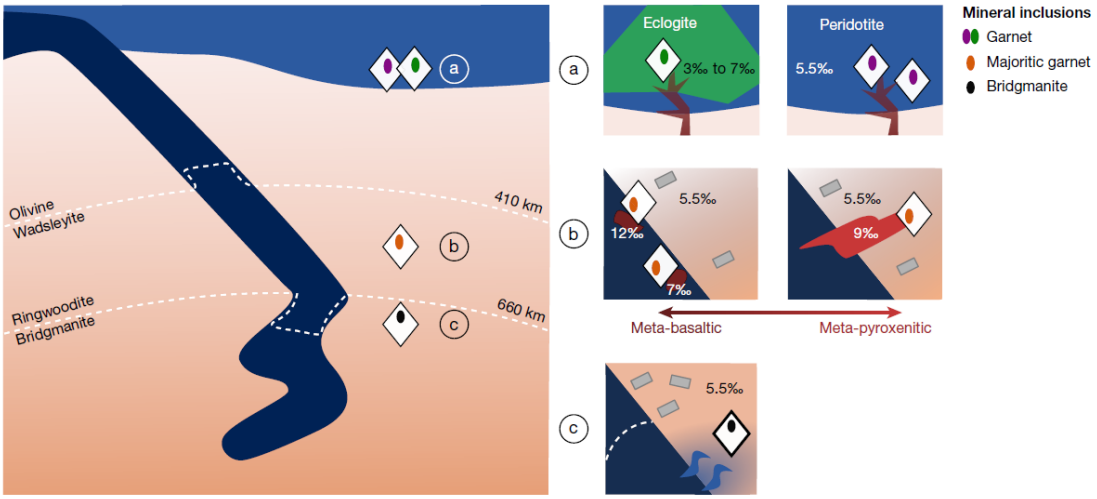

Figure 3. Model of diamond formation in the lithosphere, transition zone and lower mantle. a, Lithospheric diamond forms by fluid or melt metasomatism of eclogitic and peridotitic substrates, but the $\delta^{18}O$ value of the inclusions is buffered by the host lithology. b, In the transition zone, the carbonate-rich upper portion of a subducting slab produces carbonatitic melt. Diamonds and majoritic garnet inclusions crystallize during the interaction of the carbonatitic melt with reduced, metal-bearing convecting mantle. The short melt migration path and the limited interaction with convecting mantle produces majoritic garnet with eclogitic compositions and elevated $\delta^{18}O$, directly reflecting the local carbonated AOC melt source. Greater levels of interaction with the convecting mantle are reflected in the lower $\delta^{18}O$ and increasingly ultrabasic, meta-pyroxenitic character of some majorites. c, As the slab penetrates into the lower mantle, the negative pressure–temperature slope (the Clapeyron slope) of the post-spinel transition44 and the delayed garnet-to-perovskite transition in metabasaltic lithologies45 retards the formation of lower-mantle minerals (dotted white line). The transition to a lower-mantle mineralogy leads to slab dehydration and the hydration of the surrounding mantle. The hydrated ambient mantle releases carbon from its metallic iron hosts to form diamond.

3. 利用碎屑锆石的铕异常恢复地壳厚度的演化

翻译人：冯婉仪 fengwy@sustech.edu.cn

Tang M, Ji W Q, Chu X, et al. ***Reconstructing crustal thickness evolution from europium anomalies in detrital zircons[J]. Geology****, 2020, 49. https://doi.org/10.1130/G47745.1*

摘要：新的数据整理表明，在中酸性岩石中的锆石 Eu/Eu*值（球粒陨石标准化 Eu/$\sqrt{Sm\times Gd}$ ）与已用于推测地壳厚度的全岩 La/Yb 比值相关。锆石 Eu/Eu*值与地壳厚度之间的正相关关系可以用岩浆高压分异期间的两个过程来解释：（1）抑制斜长石结晶和（2）石榴子石的分离引起 Eu^{2+}的内生性氧化。在这里，我们根据锆石的 Eu 异常校准地壳厚度的指标。锆石 Eu/Eu*指标使得利用碎屑锆石重建岩浆弧和造山带的地壳厚度演化成为可能。为了评估这一新的指标，我们分析了从西藏南部冈底斯带现代河砂中分离出来的碎屑锆石。我们的结果揭示了自白垩纪以来的两次地壳增厚事件（至 60-70 公里）。第一次地壳增厚发生在 90-70 Ma，第二次地壳增厚发生在欧亚-印度碰撞之后（50-30 Ma）。这些发现与西藏南部沉积地层的收缩变形的时间吻合。

ABSTRACT: A new data compilation shows that in intermediate to felsic rocks, zircon Eu/Eu* [chondrite normalized Eu/$\sqrt{Sm\times Gd}$] correlates with whole rock La/Yb, which has been be used to infer crustal thickness. The resultant positive correlation between zircon Eu/Eu* and crustal thickness can be explained by two processes favored during high-pressure differentiation: (1) supression of plagioclase and (2) endogenic oxidation of Eu^{2+} due to garnet fractionation. Here we calibrate a crustal thickness proxy based on Eu anomalies in zircons. The Eu/Eu*-in-zircon proxy makes it possible to reconstruct crustal thickness evolution in magmatic arcs and orogens using detrital zircons. To evaluate this new proxy, we analyzed detrital zircons separated from modern river sands in the Gangdese belt, southern Tibet. Our results reveal two episodes of crustal thickening (to 60–70 km) since the Cretaceous. The first thickening event occurred at 90–70 Ma, and the second at 50–30 Ma following Eurasia-India collision. These findings are temporally consistent with contractional deformation of sedimentary strata in southern Tibet.

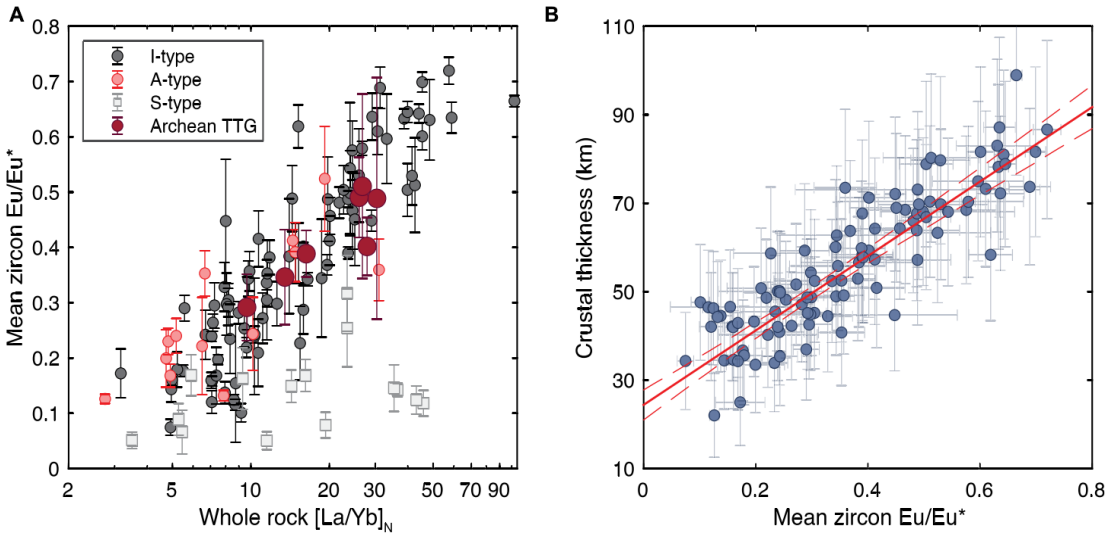

Figure 1.(A) Zircon Eu/Eu* [chondrite normalized Eu/ $\sqrt{Sm \times Gd}$] versus whole rock $[La/Yb]_N$ (N--chondrite normalized). (B) Crustal thickness–zircon Eu/Eu* regression. Each data point represents mean of multiple analyses of zircons extracted from individual rock sample. Errors are two standard errors. Linear regression (mean and 95% confidence interval shown by the solid and dashed red lines, respectively) in B was obtained using post-Archean I-type samples, post-Archean A-type samples, and Archean tonalite-trondhjemite-granodiorite (TTG) samples. Errors of crustal thickness were derived from Profeta et al. (2015).

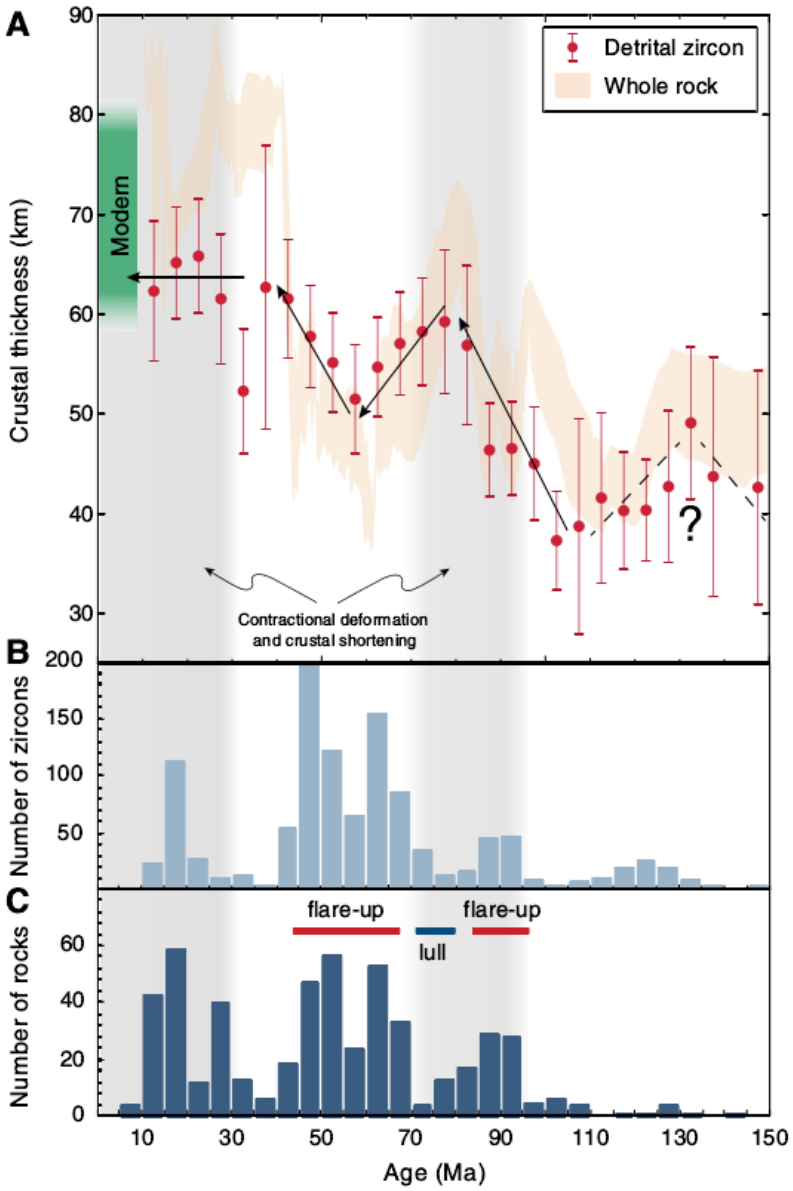

Figure 2. (A) Crustal thickness evolution of the Gangdese magmatic belt, southern Tibet, reconstructed from Eu/Eu* [chondrite normalized Eu/$\sqrt{Sm \times Gd}$] in detrital zircons (n = 1477). Data are plotted as binned averages for every 5 m.y. interval with two standard errors. Also shown here is crustal thickness calculated using the whole-rock La/Yb method (Profeta et al., 2015), plotted as running averages with two-standard-error intervals (orange band). Gangdese whole-rock La/Yb data are from Chapman and Kapp (2017). Timing of contractional deformation and crustal shortening in southern Tibet is from Kapp et al. (2007) and Leier et al. (2007). Black arrows and dashed lines illustrate the arbitrary trends of crustal thickening and thinning. (B) Age distribution of detrital zircons analyzed in this study. (C) Age distribution of Gangdese magmatic rocks compiled by Ji et al. (2014).

4. 一个连接的大西洋的诞生：磁性地层学观点

翻译人:李园洁 liyj3@sustech.edu.cn

Palcu D V, Muraszko J R, Jaqueto P F, et al. ***The birth of a connected Atlanti*** ***magnetostratigraphic perspective[J]. Frontiers in Earth Science****, 2020, 8: 375.*

https://doi.org/10.3389/feart.2020.00375

摘要：Sao Paulo 洋底高原的早古近纪的沉积物记录是理解大西洋大洋环流开启的时间和机制的关键，这对海洋-气候反馈系统具有重要影响。南大西洋联结的时间和演化过程仍未知，阻碍了理解现今环流的机制。本文中，我们为位于 Rio Grande Rise 边缘的 Sao Paulo 洋底高原上的 DSDP Site 356 的晚白垩纪到始新世的沉积物记录构建了一个改进的磁性地层年龄模型。这个模型约束大西洋环流的开始时间。我们用这个年龄模型量化沉积速率，与岩石磁学数据和发表过的地球化学数据进行比较来查明洋流重组和气候异常之间的联系。我们发现以沉积物磁学参数变化和沉积异常为特征的时期也反应在碳同位素事件中，表明大洋循环和极热事件可能存在某种联系。

ABSTRACT：The early Paleogene sedimentary record of the Sao Paulo Plateau holds the key to understanding the timing and mechanisms of the onset of Atlantic oceanic circulation, with implications for ocean – climate feedback systems. The timing and evolution of South Atlantic Ocean connectivity remain poorly understood, hindering a full understanding of modern circulation mechanisms. In this work, we develop an improved magnetostratigraphic age model for the late-Cretaceous to Eocene sedimentary record of Deep-Sea Drilling Project (DSDP) Site 356, located on the São Paulo Plateau at the edge of the Rio Grande Rise. The model constrains the timing of the beginning of Atlantic Ocean circulation, as the last obstacle to a connected Atlantic was removed. We use the age model to quantify sedimentary rates, and correlate with rock magnetic and published geochemical data to explore links between ocean current rearrangement and climatic anomalies. We find that periods characterized by variations in the magnetic properties of sediments and sedimentation anomalies in the Sao Paulo Plateau are reflected in carbon isotope events, supporting a possible link between ocean circulation and hyperthermal events.

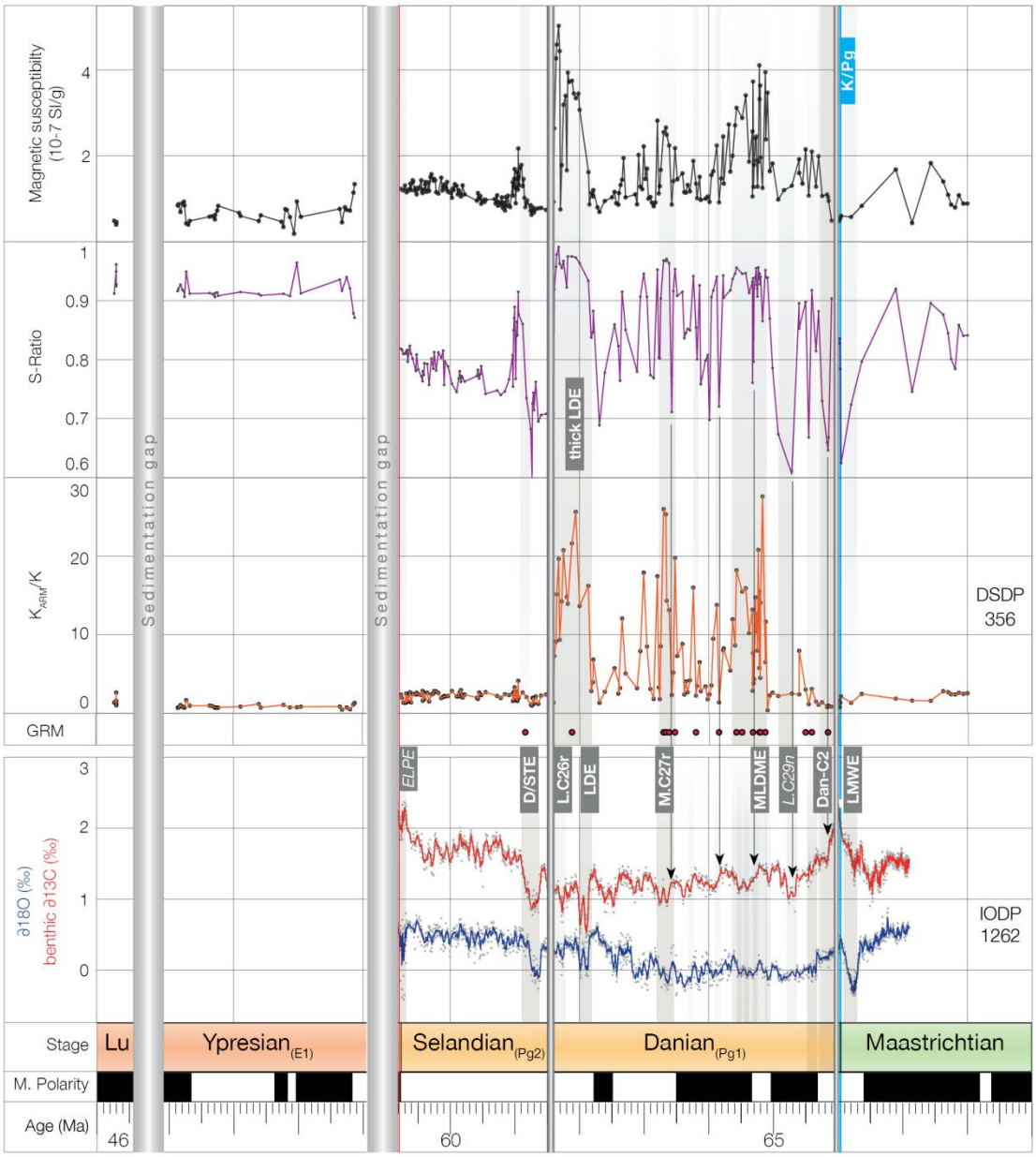

Figure 1. Stratigraphic correlations of Site 356 with global events. From the top: magnetic susceptibility and S-ratio for Deep Sea Drilling Program (DSDP) Site 356 obtained in this study, stage and magnetic polarity, and benthic d13C from Barnet et al. (2019). Marked are the major recognized events reported in the literature discussed in the text: the Cretaceous-Paleogene boundary (blue) and suspected hyperthermal-like events (red): the Cretaceous-Paleogene boundary (K/Pg), the Dan-C2 event (Dinarès-Turell et al., 2014; Jehle et al., 2015), L.C29n (Barnet et al., 2019), M.27Cr (Barnet et al., 2019), Late Danian Events (LDEs) LDE1 and LDE2 (Sprong et al., 2012; Jehle et al., 2015; Deprez et al., 2017), L.C26r (Barnet et al., 2019), Danian/Selandian Transition Event (D/STE) (Arenillas et al., 2008), Early-Late Paleocene Event (ELPE) (Coccioni et al., 2019).

5. 全新世东亚地区古地磁场方向圆度特征

翻译人：柳加波

Lund S P. ***Regional character of geomagnetic field directional circularity: Holocene East Asia[J]. Physics of the Earth and Planetary Interiors****, 2020: 106572. https://doi.org/10.1016/j.pepi.2020.106572*

摘要：这项研究总结了东亚已经发表的五个全新世古地磁长期变化曲线（PSV）的特征。每个记录都具有很高的分辨率和精确的年代。我们以 100 年为增量，等间距地插值获得了这五个记录的倾角和偏角的时间序列，并比较了它们总体上的方向变化。我们发现倾角和偏角的变化有 9 处相似的特征。这表明，在一阶上，这五个 PSV 记录都具有东亚地区一致的 PSV 特征。我们特别关注古磁方向的顺时针或逆时针运动（称为圆度）。我们使用了两种方法来估计每个 PSV 记录的方向圆度。我们首先计算了过去 3000-8000 年中每条记录的增量速率和运动方向（顺时针或逆时针），等间隔为 200 年。我们另外使用了一种更传统的技术，即在单个记录中查找可分辨的循环（从完整循环到 1/2 循环）。我们估计循环大小，持续时间和圆度方向。我们在两种计算方式中都看到了基本相同的圆度模式。在所有五个位置中，都有八个圆度振荡阶段（顺时针和逆时针）。他们通常在时间和方向圆度上具有一致性。在所有五个记录中，明显有 5 个可辨别顺时针和逆时针交替的旋回。两种圆度计算方法都表明 PSV 圆度具有振荡、跷跷板般的行为，这必须归因于地球外核中流体流动/磁通再生的模式。这种跷跷板行为是不平衡的，顺时针运动花费的时间几乎是逆时针运动时间的两倍。并且整个时间序列只有少于 10%的时间是线性（非循环）行为。方向循环往往具有大小和持续时间的分布，较小的循环持续时间较短（300-600 年），较大的循环持续时间较长（800-1500 年）。这些圆度模式的一个特征得特别注意。所有五个 PSV 记录均显示，短期（200-400 年）显著加速的圆度速率伴随着圆度方向的变化。我们看到在公元前 200 年，公元 400 年和 1300 年附近出现了这三个短暂间隔的证据。这些特征也是所有记录中常规长期变化速率最快的阶段。这些特征与高分辨率历史（<200 年）长期变化记录中异常加速的短间隔（1-2 年）地磁 Jerks 大致相似（Courtillot 和 LeMouel，1976，1984）。Gallet 等（2003）提出的证据表明，在过去约 3000 年中，PSV 内有类似的相对较短的异常加速间隔（约 102 年），他们将其称为考古地磁 jerks。我们认为我们的异常间隔与 Gallet 等（2003）的提出的 jerks 相似。

ABSTRACT: This study summarizes the pattern of directional paleomagnetic secular variation (PSV) in five previously-published Holocene records from East Asia. Each record is high in resolution and well-dated. We have developed equi-spaced (100-year increment) time series for the declinations and inclinations for the five sites and compared their overall directional variability. We see evidence of nine correlatable scalar features in both inclination and declination. These comparisons suggest that, to first order, these five PSV records all estimate the same regional pattern of PSV for East Asia. We specifically focus on the clockwise or counter-clockwise motion of paleomagnetic directions (termed circularity) in these PSV records. We have used two techniques to estimate the directional circularity of each PSV record. We have first calculated the incremental rate and direction of motion (clockwise or counter-clockwise) in 200-year increments for each record over the last 3000–8000 years. We have separately used a more traditional technique of looking for discernable looping (full loops down to 1/2 loops) in individual records. We estimate the loop sizes, durations, and circularity direction. We largely see the same pattern of circularity in both measurement techniques. There are eight intervals of oscillating circularity (clockwise versus counter-clockwise) in all five sites. They generally agree in timing and direction of circularity. We see evidence for 5 discernable loops alternating between clockwise and counter-clockwise in all five records. Both techniques suggest an oscillating, teeter-totter like, behavior to PSV circularity that must be due to the pattern of fluid flow/magnetic flux regeneration in the outer core. This teeter-totter behavior is unbalanced with almost twice the time spent in clockwise motion as in counter-clockwise motion. Less than 10% of the overall time series duration is spent in linear (not circulating) behavior. The loops tend to have a distribution of sizes and durations with smaller loops being shorter in duration (300–600 years) and bigger loops having longer durations (800–1500 years). One particular feature of these circularity patterns bears special note. All five PSV records show short-term (200–400 years) significant acceleration in circularity rate combined with change in circularity direction. We see evidence for three of these short intervals near 200 BCE, 400 CE, and 1300 CE. These features also are intervals of the fastest regular secular variation rates in all the records. These features are broadly analogous to geomagnetic jerks (Courtillot and LeMouel, 1976, 1984) in that they are short intervals (1–2 years) of anomalous acceleration within high-resolution

historical (<200 yr) secular variation records. Gallet et al. (2003) showed evidence for similar relatively short anomalous acceleration intervals (~102 years) within PSV for the last ~3000 years, which they termed archeomagnetic jerks. We think our anomalous intervals are comparable to those of Gallet et al. (2003).

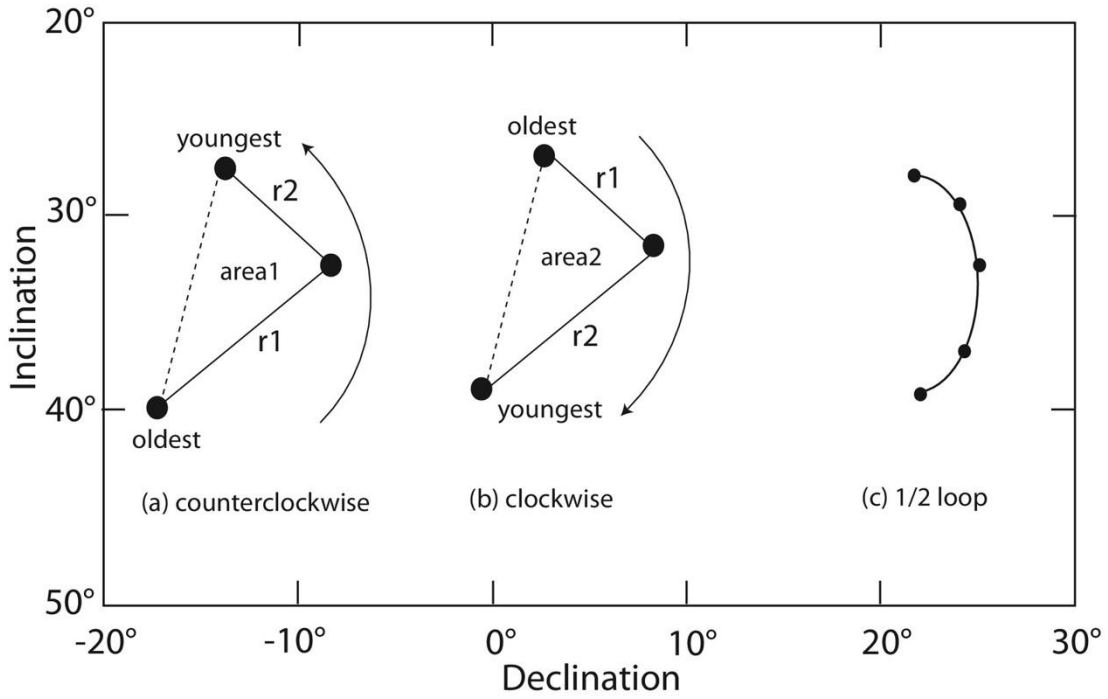

Fig 1: Graphical representation of the methodology used to calculate true circularity rates (a, b) and looping patterns (c). Areas of looping in a and b are measured in arc degrees squared (area).

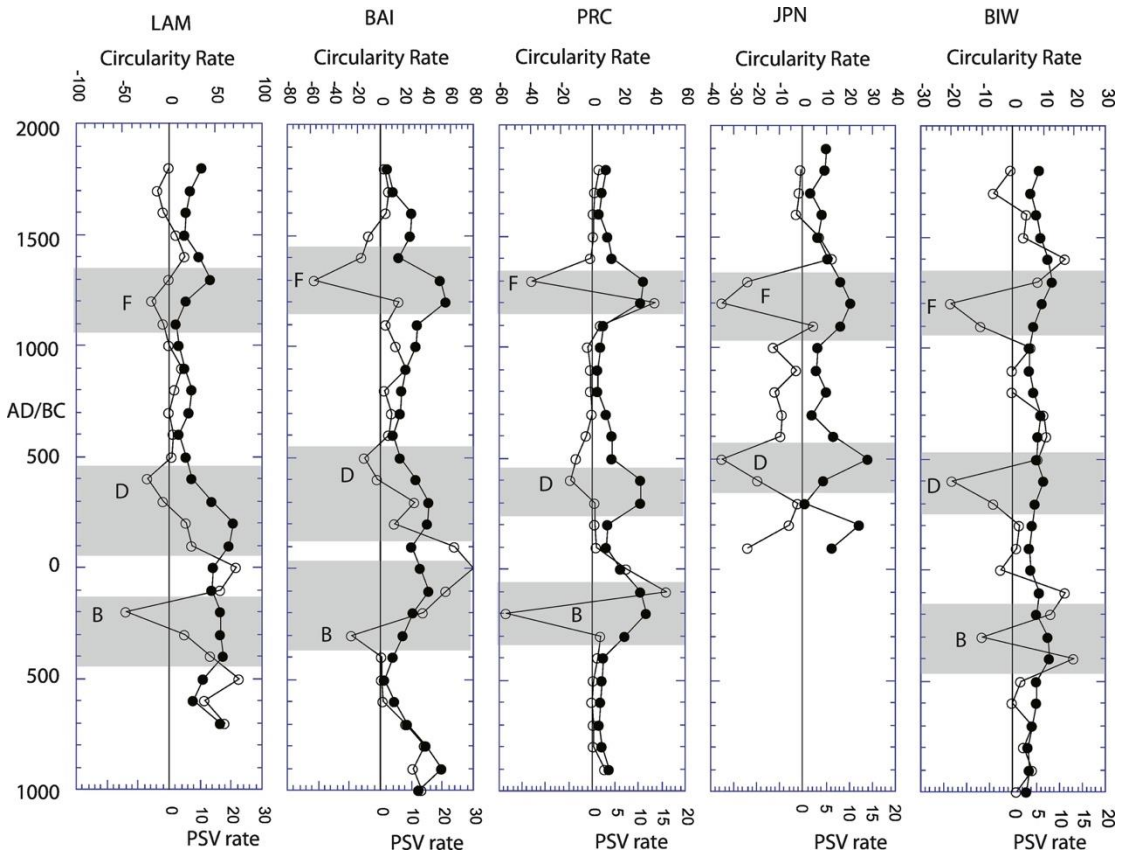

Fig 2: Comparison of true circularity rate (arc degree squared, 3-pt average, open circles) with absolute interval secular variation rate (arc degrees over same interval as circularity) irrespective of directional circularity.

6. 古雅浦弧-卡洛琳板块碰撞和俯冲再生的地球化学和年代证据

*Zhang J , Zhang G . **Geochemical*** **翻译人：刘伟 inewway@163.com** ***and al evidence for collision of proto-Yap arc/Caroline plateau and rejuvenated plate subduction at Yap trench[J]. Lithos**, 2020:105616.* https://doi.org/10.1029/2019JB018610

摘要：雅浦弧被认为是从古雅浦-IBM 弧系统衍生出来的。这是罕见的以变质岩为主的短距离弧沟特征的洋底高原俯冲的例子，其不同于 IBM 弧系统。然而，雅浦弧基底岩石的起源和形成时间尚不清楚。本研究首次提供了雅浦弧变质基底岩(角闪岩)的放射性年龄及全岩主量元素、微量元素和 Sr–Nd-Pb–Hf 同位素分析结果。根据岩石的主要元素组成和微量元素组成，可以将岩石样品分为三类。第 1 组样品具有极其亏损型微量元素模式和 Dupal 型同位素特征，代表了来源于初始雅浦弧前玄武岩（FABs）。第 2 组样品具有碱性洋岛玄武岩的富集型微量元素特征和太平洋型地幔特征，代表了来源于卡罗琳高原的玄武岩。第 3 组样品具有典型的成熟岛弧火山岩 Nb–Ta–Zr–Hf 负异常特征，代表了来源于原始雅浦岛弧火山岩。通过角闪石 40Ar/39Ar 定年和离子探针（SIMS）进行榍石 U-Pb 定年，这些角闪岩形成于 21 Ma，记录了卡洛琳高原与古雅普弧碰撞事件的发生时间。我们认为，雅浦弧在这次碰撞后从 IBM 弧演变而来。这些岩石由于古雅普弧与卡洛琳高原的碰撞而变质，形成了现在的雅普弧。根据年龄测定和地球化学的结果，我们提出雅浦弧的构造演化的三阶段模型: 卡洛琳板块俯冲的早期阶段(原雅浦岛弧火山岩形成)，原雅浦岛弧与卡洛琳高原的碰撞阶段（雅浦岛弧变质岩形成），卡洛琳高原向雅浦海沟的超慢速俯冲阶段（伴随强烈俯冲侵蚀，以及年轻岛弧火山岩的产生）。

ABSTRACT: The Yap Arc was considered to have derived from the proto-Yap-Izu Bonin-Mariana arc system. It is a rare example of subduction of an oceanic plateau with short arc–trench distance and consists mainly of metamorphic rocks, which are distinct from the Izu Bonin-Mariana arc system. However, it is not known on the origin and formation time of the basement rocks of the Yap Arc. For the first time, in this study we provide the results of radiometric age-dating and whole-rock major element, trace element and Sr–Nd-Pb–Hf isotope analyses for the metamorphic basement

rocks (amphibolites) of the Yap Arc. These rock samples can be classified into three groups based on their major and trace element compositions. Group 1 samples have strong depletion of LREEs and a Dupal-type isotopic signature, and they represent forearc basalts (FABs) of the nascent Yap forearc. Group 2 samples have an alkali basalt-like geochemistry and oceanic island basalts (OIBs) type trace element patterns, and they represent the basalts of the Caroline Plateau. Group 3 samples have island-arc-type negative anomalies of Nb–Ta–Zr–Hf, and they may represent the volcanic rocks of the proto-Yap Arc. These amphibolites were formed at 21 Ma according to 40Ar/39Ar amphibole dating and in situ SIMS U-Pb titanite dating, and they record the timing of the collisional event between the Caroline Plateau and the proto-Yap Arc. We propose that the Yap arc has been evolving distinctly from the Izu-Bonin-Mariana Arc since this collision time. These rocks were metamorphosed and brought onto the present Yap Arc as a result of the collision between the proto-Yap Arc and the Caroline Plateau. Based on the new results of age-dating and geochemistry of this study, we propose three stages of tectonic evolution for the Yap Arc as a result of collision from the Caroline plateau: an early stage (proto-Yap Arc) of subduction of the Caroline Plate, collision of the proto-Yap Arc with the in-coming young Caroline Plateau, and rejuvenated plate subduction at the Yap Trench with limited volcanism.

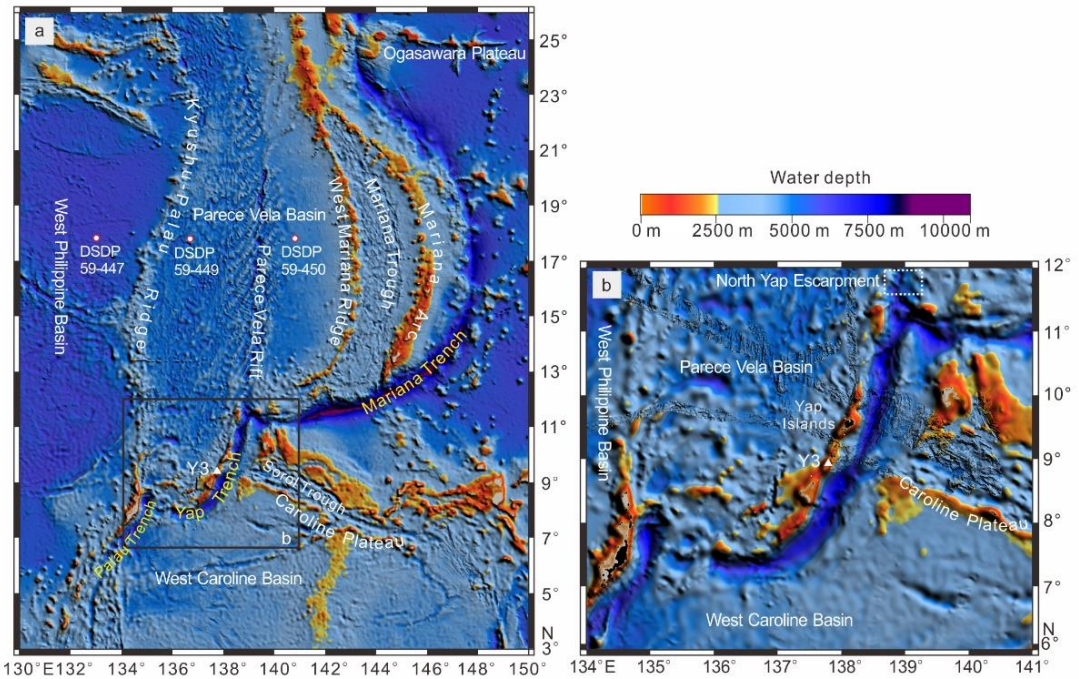

Figure 1. Geological and bathymetric map of the Yap Arc–Trench system in the west Pacific.

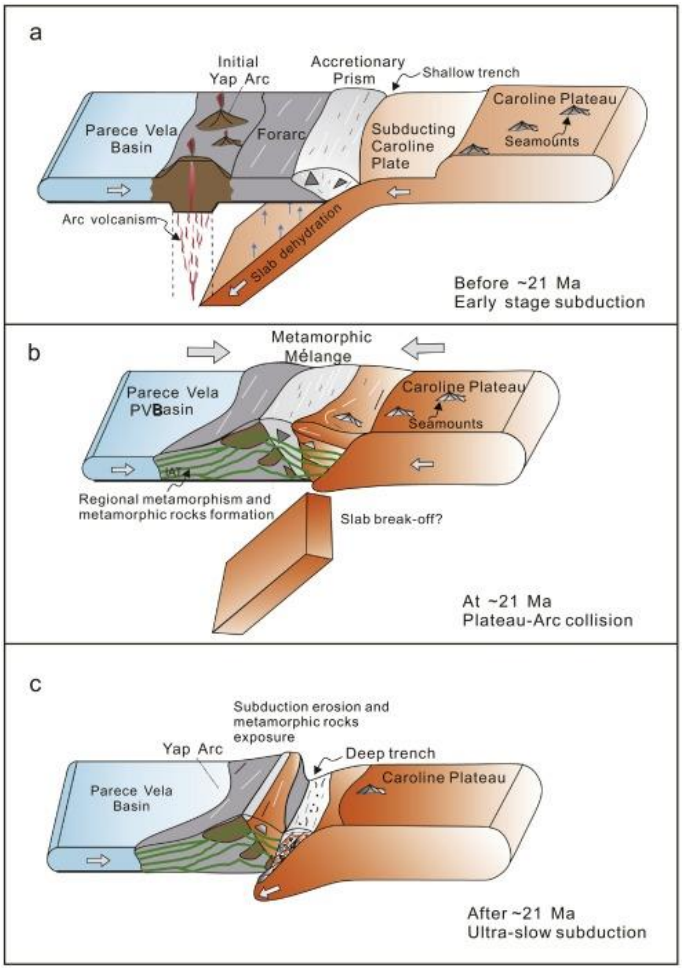

Figure 2. Model of the tectonic evolution of the Yap Arc. (a) Early stage subduction of the Caroline Plate and the initial-Yap Arc. Parts of the subducting plate, including oceanic crust, igneous seamounts, and overlying sediments were scraped off and accreted into the Accretionary Prism in the Yap forearc. (b) Collision of the initial-Yap Arc with the in-coming Caroline Plateau at ~21 Ma. The nascent-Yap Arc (island-arc tholeiites), the initial Yap forearc (FABs), the accreted Caroline Plateau (OIBs) were brought together and metamorphic mélanges are generated during the regional metamorphism caused by the collision. This collision also caused the temporary cessation of the Yap Arc volcanism, shortening the forearc and clogging of the Yap Trench. (c) Rejuvenated but ultra-slow subduction at the present Yap Trench with limited volcanic activity on the Yap Arc. The ultra-slow subduction of the buoyant Caroline Plateau would have caused an elevated rate of erosion above the Yap subduction zone, which in turn caused the exhumation of the amphibolite-facies metamorphic rocks onto the present-day Yap Arc, as

well as its embryonic arc morphology with a short arc–trench distance. The ultra-slow subduction probably explains the scarce volcanism at 11– 7 Ma in the Yap Trench.

7. 3.6Ma 亚洲中纬度干旱化和西风带历史与全球气候变冷有关

翻译人：曹伟 11930854@QQ.com

Fang X.M., An Z.S.,

Clemens S.C., et al., ***The 3.6-Ma aridity and westerlies history over midlatitude Asia linked with global climatic cooling****. [J].* ***PNAS****, 2020.*

www.pnas.org/cgi/doi/10.1073/pnas.1922710117

摘要：亚洲中纬度地区（MLA）受西风带控制，是全球大气沙尘的主要来源，在地球气候系统中占有重要地位。然而，目前还不清楚西风带、MLA 干旱化和来自该地区的沙尘通量是如何随时间演变的。本文我们研究了一批特有的高分辨率风成尘记录，覆盖了过去 3.6 Ma 时间序列，这是从塔克拉玛干沙漠南缘（迄今为止 MLA 内部最厚的黄土钻孔序列 671m）中获得的。研究结果表明，与干旱和西风带密切相关的风积沙尘指示了干燥气候、沙漠化和稳定的地表，促进了至少 3.6 Ma 以来黄土的持续沉积。该区域在 2.7、1.1 和 0.5 Ma 经历了长期的逐步干燥，在 1.1 Ma 和 0.5 Ma 之间，主要周期从 41ka 周期性转变到 100ka 周期性。这些特征在时间域和频率域（包括中更新世过渡期）与全球冰量变化很好地吻合，突出了这些时间尺度上的全球变冷驱动干旱和西风带气候变化。数值模拟表明，全球降温可以使 MLA 变干，增强西风带，有利于沙尘的排放和输送，提供了一个解释框架。增加的粉尘可能促进了正反馈（例如，降低大气二氧化碳浓度和调节辐射预算），有助于进一步冷却。揭开 MLA 干旱和西风带气候的长期演变是揭开全球气候变化之谜不可缺少的组成部分。

ABSTRACT: Midlatitude Asia (MLA), strongly influenced by westerlies-controlled climate, is a key source of global atmospheric dust, and plays a significant role in Earth s climate system. However, it remains unclear how the westerlies, MLA aridity, and dust flux from this region evolved over time. Here, we report a unique high-resolution eolian dust record covering the past 3.6 Ma, retrieved from the thickest loess borehole sequence (671 m) recovered to date, at the southern margin of the Taklimakan desert in the MLA interior. The results show that eolian dust accumulation, which is closely related to aridity and the westerlies, indicates existence of a dry climate, desert area, and stable land surface, promoting continuous loess deposition since at least 3.6 Ma. This region experienced long-term stepwise drying at 2.7, 1.1, and 0.5 Ma, coeval with a dominant periodicity

shift from 41-ka cyclicity to 100-ka cyclicity between 1.1 Ma and 0.5 Ma. These features match well with global ice volume variability both in the time and frequency domains (including the Mid-Pleistocene Transition), highlighting global cooling-forced aridity and westerlies climate changes on these timescales. Numerical modeling demonstrates that global cooling can dry MLA and intensify the westerlies, which facilitates dust emission and transport, providing an interpretive framework. Increased dust may have promoted positive feedbacks (e.g., decreasing atmospheric CO2 concentrations and modulating radiation budgets), contributing to further cooling. Unraveling the long-term evolution of MLA aridity and westerlies climate is an indispensable component of the unfolding mystery of global climate change.

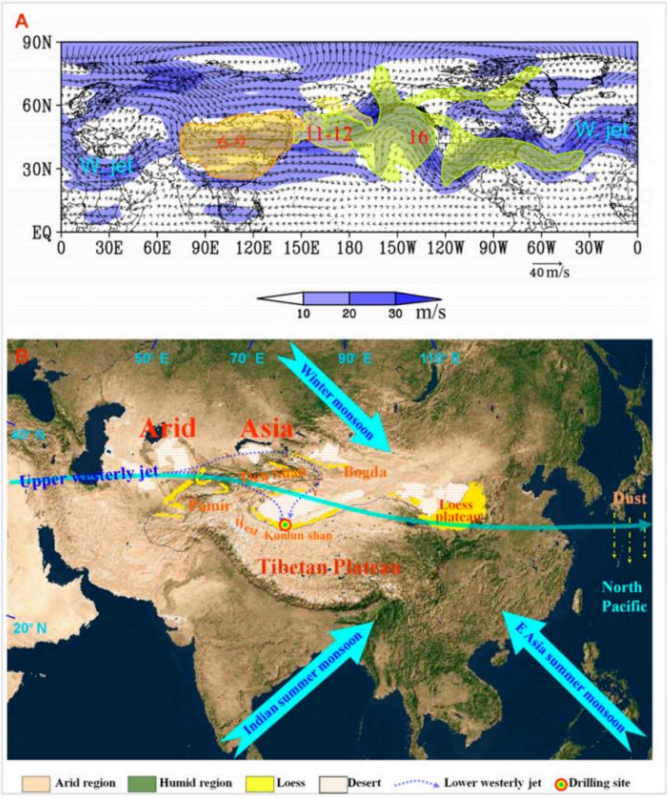

Figure 1. (A) The long-distance transport of a dust storm in NH MLA on April 6–9, 2001, via the westerly jet as indicated by the strongest wind speeds in the 500-hPa map of the potential height and vector winds. Red numbers are dates. Black solid lines stand for the potential height, and arrows stand for wind direction (modified from ref. 8). (B) Physical geography and schematic atmospheric circulation pattern of Asia with the locations of the loess drilling site. Note that MLA is the largest arid interior region in a temperate continent (pale area) and that East Asia is characterized by a monsoonal humid region (green area). The solid black line outlines the 3,000-m-altitude region.

8. 从石笋 $\delta^{18}O$ 获得的印度夏季风 —— 一篇综述

翻译人：杨会会 11849590@mail.sustech.edu.cn

Kaushal N, Breitenbach S F M, Lechleitner F A et al., ***The Indian Summer Monsoon from a Speleothem Perspective —— A Review [J].Quaternary****, 2018, 1, 29.*

https://doi.org/10.3390/quat1030029

摘要：作为最显著的季节性循环大气环流模式之一，亚洲夏季季风(ASM)的变化显著影响着东亚地区的水文气候，也影响着东亚地区居住的全球近三分之一人口的社会经济。ASM 强度和季节性的变化对 ASM 区有显著影响，但变化的驱动因素和不同区域对 ASM 的响应尚不清楚。在过去的二十年里，许多研究基于石笋指标如氧同位素重建了 ASM。这些重建使人们对 ASM 的驱动因素和响应有了初步解释，增加了季风的可预测性。在这篇综述文章中，我们着重研究了印度季风区近端的印度石笋 $\delta^{18}O$ 记录。印度的石笋 $\delta^{18}O$ 记录具有精准的定年，显示出 ASM 在轨道上至数百年时间尺度上，响应主导驱动因素的高振幅变化。我们研究了 SISAL_v1 数据库中的印度石笋记录，并为数据库提供不同气候状态下的记录质量和区域气候解释概述。我们强调并建议使用数据模型比较、光谱分析方法、多指标调查和监测等工具在最有用的时间段(气候事件)和位置，进行进一步工作。

Abstract: As one of the most prominent seasonally recurring atmospheric circulation patterns, the Asian summer monsoon (ASM) plays a vital role for the life and livelihood of about one-third of the global population. Changes in the strength and seasonality of the ASM significantly affect the ASM region, yet the drivers of change and the varied regional responses of the ASM are not well understood. In the last two decades, there were a number of studies reconstructing the ASM using stalagmite-based proxies such as oxygen isotopes ($\delta^{18}O$). Such reconstructions allow examination of ASM drivers and responses, increasing monsoon predictability. In this review paper, we focus on stalagmite $\delta^{18}O$ records from India at the proximal end of the ASM region. Indian stalagmite $\delta^{18}O$ records show well-dated, high-amplitude changes in response to the dominant drivers of the ASM on orbital to multi-centennial timescales, and indicate the magnitude of monsoon variability in response to these drivers. We examine Indian stalagmite records collated in the Speleothem Isotope

Synthesis and Analysis version 1(SISAL_v1) database and support the database with a summary of record quality and regional climatic interpretations of the $\delta^{18}O$ record during different climate states. We highlight current debates and suggest the most useful time periods (climatic events) and locations for further work using tools such as data-model comparisons, spectral analysis methods, multi-proxy investigations, and monitoring.

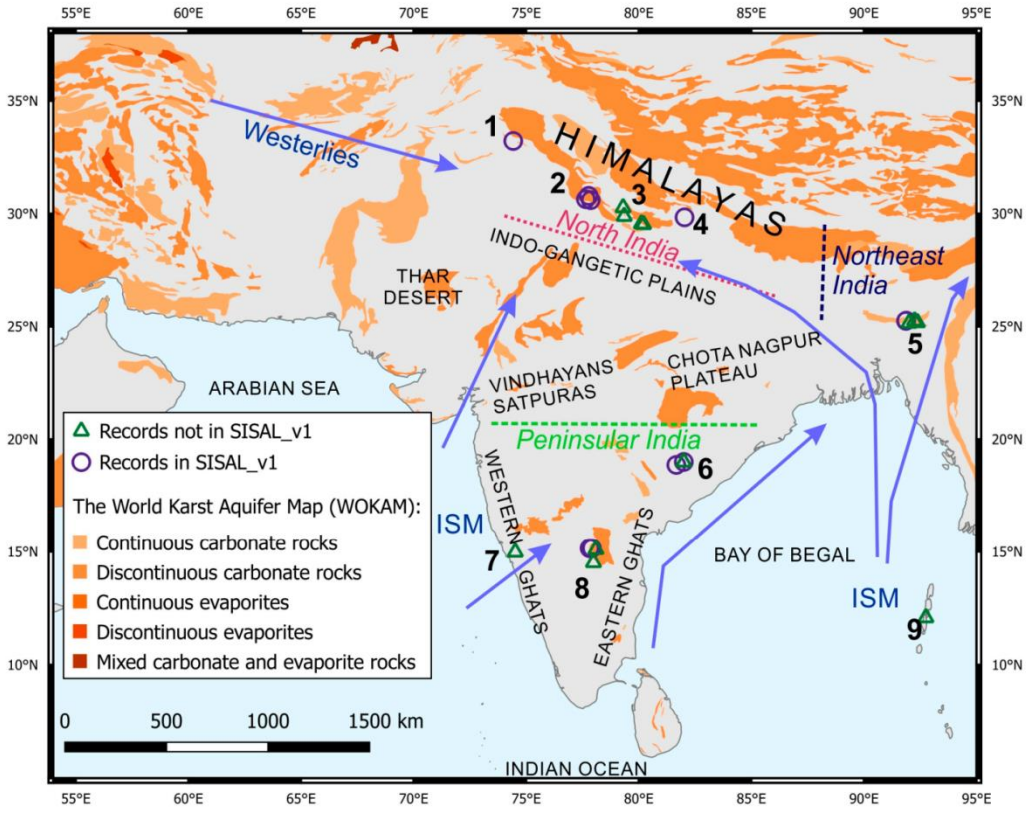

Figure 1. Study area with carbonate rock distribution as given by the World Karst Aquifer Map (WoKAM [42]) (see map legend), generalized wind directions (Indian summer monsoon (ISM) and westerlies marked by blue arrows), geographical features, regions (north, northeastern, and peninsular India) and cave locations (1: Kalakot; 2: Bittoo, Sahiya, Tityana; 3: Chulerasim, Dharamjali, Panigarh, Sainji; 4: Timta; 5: Mawmluh, Rupasor, Syndai, Umsynrang, Wah Shikhar; 6: Dandak, Jhumar, Kotumsar; 7: Akalagavi; 8: Belum, Munagamanu, Nakarallu, Valmiki；9：Baratang).

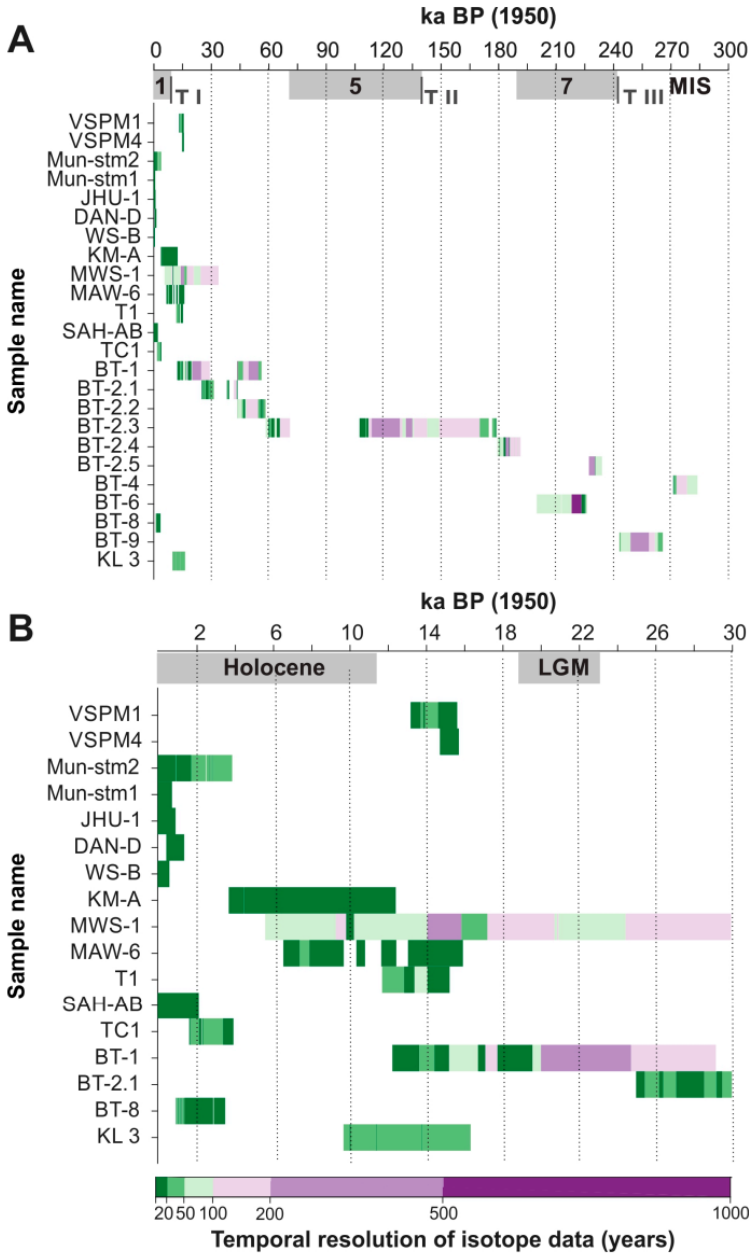

Figure 2. Temporal distribution of stalagmite $\delta^{18}O$ records from India in the Speleothem Isotope Synthesis and AnaLysis database version 1 (SISAL_v1). Age in ka before present (BP) is given on the *x*-axis. The two figures cover (A) 300 to 0 ka BP, and (B) 30 to 0 ka BP. The color bar indicates the temporal resolution of isotopic data (years). The *y*-axis gives the record's identifier (ID; entity_name) in the database. VSPM1 and VSPM4, Valmiki cave; Mum-stm2 and Munstm-1, Munagamanu cave; JHU-1, Jhumar cave; DAN-D, Dandak cave; WS-B, Wah Shikhar cave; KM-A, MWS-1, and MAW-6, Mawmluh cave; T1, Timta cave; SAH-AB, Sahiya cave; TC1, Tityana cave; BT-1 to BT-9, Bittoo cave; KL3, Kalakot cave. Further details can be found in Table 1.

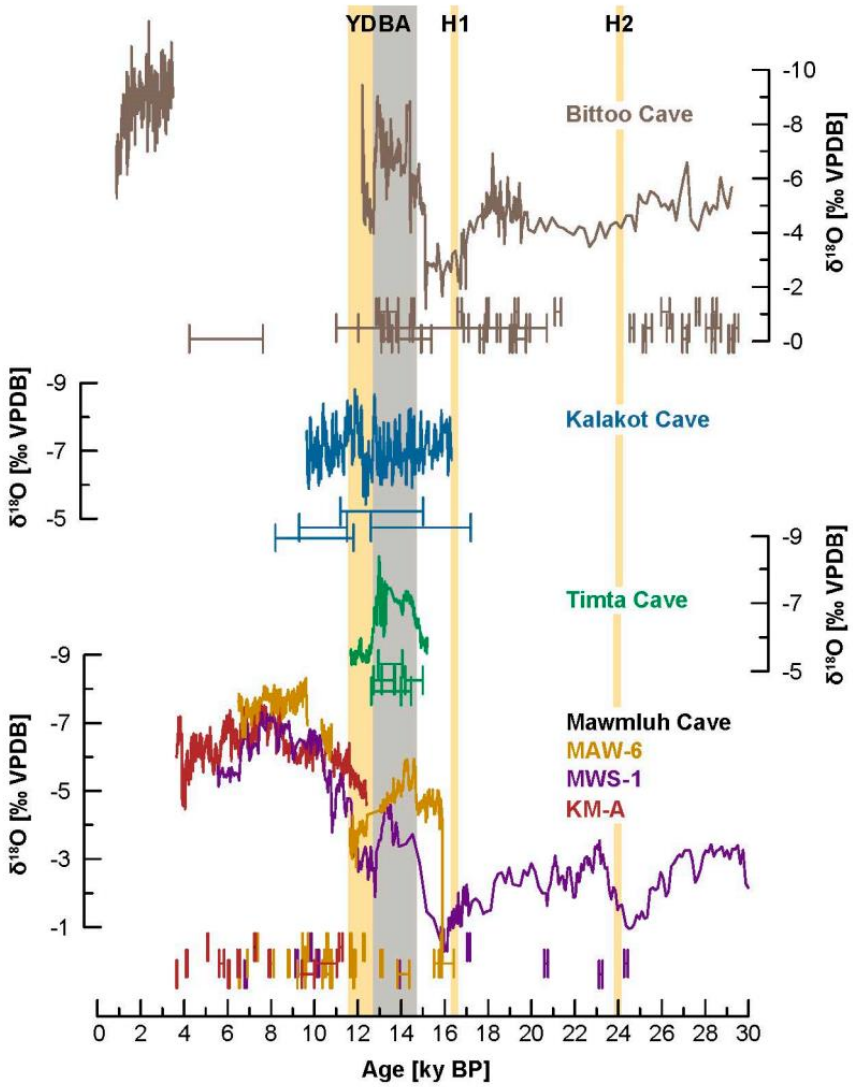

Figure 3. SISAL_v1 ISM stalagmite $\delta^{18}O$ records covering millennial events over the last deglaciation. The Younger Dryas (YD) and Heinrich events 1 and 2 [118] are indicated by yellow bars. Bölling–Allerød (BA) is indicated by a grey bar. The BA–YD transition is marked at 12.8 ka BP in the figure (GISP2 [119]). Bittoo [13], Kalakot [44], Timta [15], and Mawmluh [16,17] records are shown along with their U-Th age errors.

9. 中国东海陆源沉积物供给的气候驱动变化

翻译人：王敦繁 dunfan-w@foxmail.com

Anderson, C. H., Murray, R. W., Dunlea, A. G., Giosan, L., Kinsley, C. W., McGee, D., & Tada, R. ***Climatically driven changes in the supply of terrigenous sediment to the East China Sea. Geochemistry, Geophysics, Geosystems,*** *2018,19, 2463–2477.*

https://doi.org/10.1029/2017GC007339

摘要：我们研究了近 400kyr 的古海洋沉积记录，这些记录来自于东中国海两个地点的沉积物中的主要、微量和稀土元素，这些沉积物是在“远征 346”海洋钻井项目中钻探的。利用多元统计分区技术(Q-mode factor analysis、多元线性回归)，对五个地壳源成分(陆上地壳(UCC)、洛川黄土、下树黄土、日本南部岛屿、九州火山)进行了识别和量化，并对其质量累积率(MARs)进行了建模。UCC(陆源贡献 35-79%)和洛川黄土(贡献 16-55%)在时间上是最丰富的端部成员，而下树黄土、日本南部岛屿和九州火山岩(贡献 1-22%)是最丰富的端部成员。UCC 和洛川黄土火星的旋回可能表明大陆和泥质物质被主要河流输送到冲绳海槽。海平面和颗粒粒度(如 SiO2/Al2O3)的增加与日本南部岛屿的通量增加相一致，表明沉积物来自日本。陆源破坏总量的增加比最低相对海平面早几千年，这可能表明大陆架物质的迁移。这些包体的相对贡献的变化与总 3 月,指示成分变化的沉积物堆积速率变化明显不同,但可能与海平面的变化,河边的风成通量,在冰期间冰期主要以自我传输为主,复杂的精确的季风重建以河流沉积物为主。

ABSTRACT: We examine the paleoceanographic record over the last 400 kyr derived from major, trace, and rare earth elements in bulk sediment from two sites in the East China Sea drilled during Integrated Ocean Drilling Program Expedition 346. We use multivariate statistical partitioning techniques (Q-mode fac- tor analysis, multiple linear regression) to identify and quantify five crustal source components (Upper Con- tinental Crust (UCC), Luochuan Loess, Xiashu Loess, Southern Japanese Islands, Kyushu Volcanics), and model their mass accumulation rates (MARs). UCC (35–79% of terrigenous contribution) and Luochuan Loess (16–55% contribution) are the most abundant end-members through time, while Xiashu Loess, South- ern Japanese Islands, and Kyushu Volcanics (1–22% contribution) are the lowest in abundance when present. Cycles in UCC and Luochuan Loess MARs may indicate continental and loess-like material transported by major rivers into the

Okinawa Trough. Increases in sea level and grain size proxy (e.g., SiO2/Al2O3) are coincident with increased flux of Southern Japanese Islands, indicating localized sediment supply from Japan. Increases in total terrigenous MAR precede minimum relative sea levels by several thousand years and may indicate remobilization of continental shelf material. Changes in the relative contribution of these end-members are decoupled from total MAR, indicating compositional changes in the sediment are distinct from accumulation rate changes but may be linked to variations in sea level, riverine and eolian fluxes, and shelf-bypass processes over glacial-interglacials, complicating accurate monsoon reconstructions from fluvial dominated sediment.

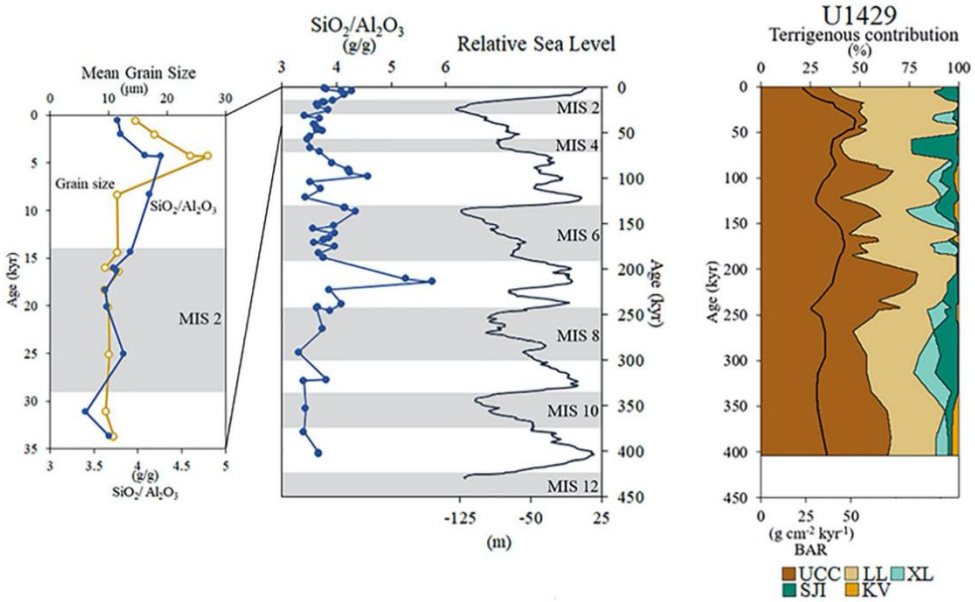

Figure 1. (left) Grain size proxy SiO2/Al2O3 ratio (g/g, blue line with closed circles) presented with relative sea level (black line) (Spratt & Lisiecki, 2016) over the last 450 kyr. Mean grain size (lm) from Zhao et al. (2017) (yellow line with open circles) and SiO2/Al2O3 are compared over the last 34 kyr. The y-axis is age (kyr) and horizontal shaded regions indicate glacial periods (Lisiecki & Raymo, 2005). (right) Comparison of Bulk Accumulation Rate (BAR, g cm22 kyr21) and terrigenous contribution (%). BAR is plotted as the solid black line. The end-member contributions are plotted to sum to 100%, with each color representing the sum of each end- member contribution plus the end-members to the left. The total terrigenous fraction is dominated by the UCC-like end-member.

10. 6500 年以来风暴活动对气候突变的纬度响应

翻译人：李海 12031330@mail.sustech.edu.cn

Yang, Y., Maselli, V., Normandeau, A., Piper, D. J. W., Li, M. Z., Campbell, D. C., et al. **Latitudinal response of storm activity to abrupt climate change during the last 6,500 years [J].** ***Geophysical Research Letters***,2020, 47, e2020GL089859.

https://doi.org/10.1029/2020GL089859

摘要：基于来自 Scotian Shelf(加拿大东部)6.5 kyr 的大风暴新记录，提供了来自中纬度的第一个 3.5 ka 的记录，研究了大西洋经向翻转环流(AMOC)的强度对北大西洋不同纬度风暴的影响。与其他史前风暴记录的汇编对比表明，在低纬度和中纬度之间，风暴峰值有时是同步的(4.5-2.5 ka 和 0.5 ka 之后)，但在其间(2.5-0.5 ka)在纬度上是不同步的。同步(异步)行为与 AMOC 的持续增加(减少)相关。自 2.5 ka 以来，低纬度和中纬度地区之间的风暴活动变化更加频繁，这与气候突变频率的增加有关。这些发现表明了由气候突变引起的风暴活动的纬向响应，这对于正确评估北大西洋海岸线未来的风暴风险至关重要。

Abstract： This study examines the influence of the strength of Atlantic Meridional Overturning Circulation (AMOC) on storminess at different latitudes in the North Atlantic, based on a new 6.5 kyr record of large storms from the Scotian Shelf (Eastern Canada) that provides the first >3.5 ka record from mid-latitudes. Comparison with a compilation of other paleo-storm records shows that peaks in storminess are at times synchronous (4.5-2.5 ka and since 0.5 ka) between low- and mid-latitudes, but in the intervening period (2.5-0.5 ka) were latitudinally asynchronous. Synchronous (asynchronous) behaviour correlates with sustained increase (decrease) of AMOC. Regime shifts in storm activity between low- and mid-latitudes were more frequent since 2.5 ka, related to increased frequency of abrupt climate changes. These findings indicate a latitudinal response of storm activity due to abrupt climate change, which is critical to correctly assess future storm risks along the North Atlantic coastline.

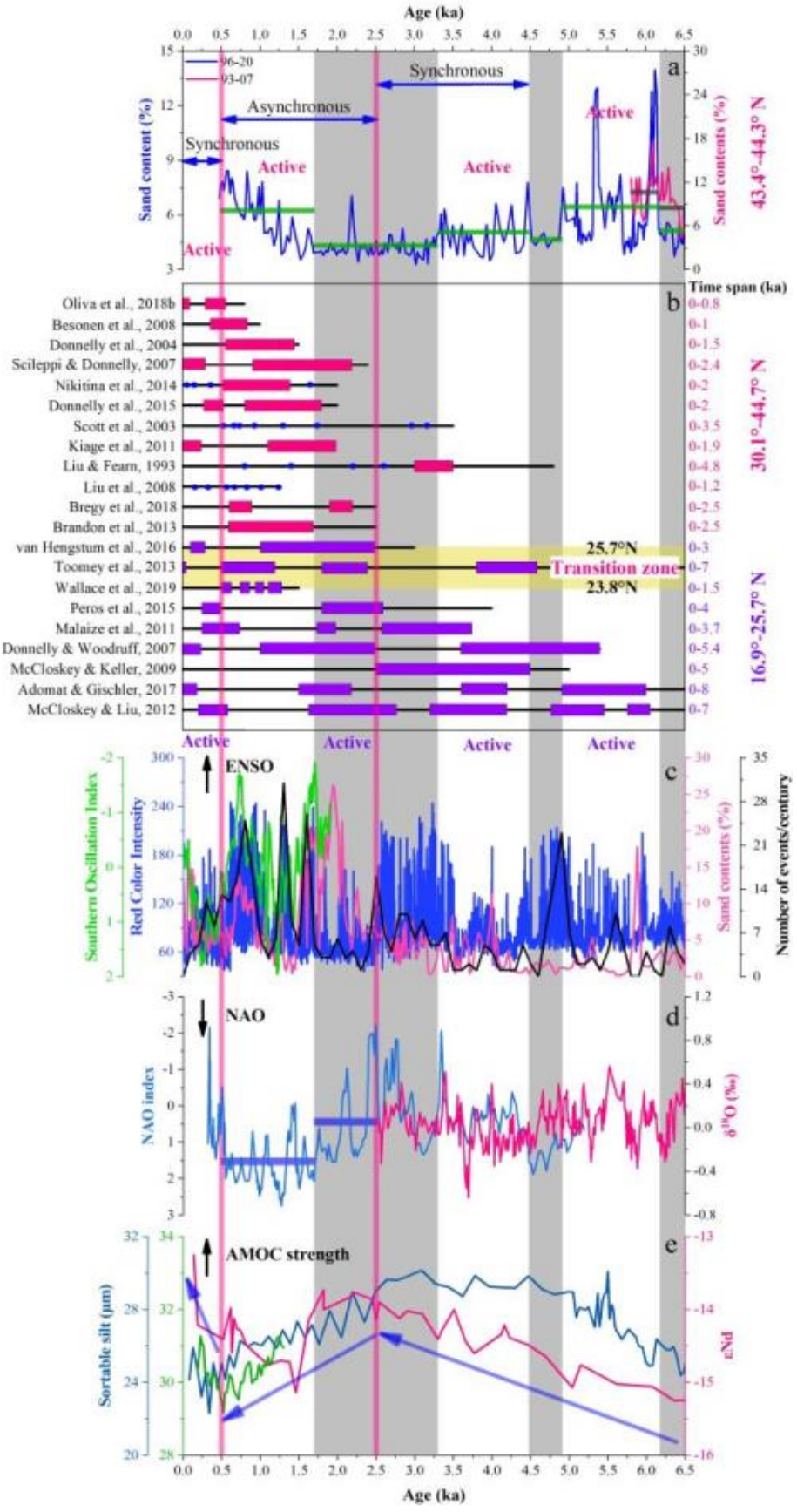
Age (ka)
96-20
93-07
Synchronous
Asynchronous
Synchronous
Active
Active
Active
Active
Sand content (%)
Sand contents (%)
43.4°-44.3° N
a
Time span (ka)
Oliva et al., 2018b
Besonen et al., 2008
Donnelly et al., 2004
Scileppi & Donnelly, 2007
Nikitina et al., 2014
Donnelly et al., 2015
Scott et al., 2003
Kiage et al., 2011
Liu & Fearn, 1993
Liu et al., 2008
Bregy et al., 2018
Brandon et al., 2013
van Hengstum et al., 2016
Toomey et al., 2013
Wallace et al., 2019
Peros et al., 2015
Malaize et al., 2011
Donnelly & Woodruff, 2007
McCloskey & Keller, 2009
Adomat & Gischler, 2017
McCloskey & Liu, 2012
25.7°N
Transition zone
23.8°N
30.1°-44.7° N
16.9°-25.7° N
b
Active
Active
Active
Active
ENSO
Southern Oscillation Index
Red Color Intensity
Sand contents (%)
Number of events/century
c
NAO
NAO index
δ18O (‰)
d
AMOC strength
Sortable silt (μm)
εNd
e
Age (ka)

Figure. 1 Comparison of storm reconstruction with other paleoclimatic proxies in the North Atlantic. (a) Sand contents from cores 96-20 and 93-07. The average sand content at each stage is shown in green and black bars. (b) A compilation of storm reconstruction from different latitudes (Table S1). Red and purple bars and blue dots indicate periods of frequent storms. The truncated black horizontal lines represent the time period covered by each study. The yellow bar shows the transition zone between the recurving and non-recurving storms. (c) ENSO reconstructions from Laguna Pallcacocha, Ecuador (Red Color Intensity and Number of events/century; Moy et al., 2002), El Junco Lake, Galapagos (Sand contents; Conroy et al., 2008) and the equatorial Pacific (Southern Oscillation Index; Yan et al., 2011). (d) NAO reconstructions from southwestern Greenland (NAO index; Olsen et al., 2012) and northwest Africa (δ 18O; Wassenburg et al., 2016). (e) Reconstructed AMOC strength from Labrador - Baffin Bay region (mean size of the sortable silt; Rashid et al., 2017; Thornalley et al., 2018), and Bermuda Rise (εNd; Lippold et al., 2019). Blue arrows show the abrupt transitions in AMOC strength during the mid-to-late Holocene. Gray bars indicate decreased storm activity in Eastern Canada and red bars mark shifts in storm frequency pattern around 2.5 ka and 0.5 ka in the North Atlantic.

11. 过去 700 kyr 热带太平洋西北部温跃层变化动力学

翻译人：张亚南 zhangyn3@mail.sustech.edu.cn

Qi jia, Tiegang Lie, Zhifang Xiong et al., ***Thermocline dynamics in the northwestern tropical Pacific over the past 700 kyr [J]. Quaternary Science Reviews****, 2020, 244. 106465.*

https://doi.org/10.1016/j.quascirev.2020.106465

摘要：温跃层环境条件的变化对西太平洋暖池（WPWP）演化，以及对太平洋低纬和中高纬地区的联系都具有重要的作用。但是，WPWP 西北部温跃层的变化及其驱动机制却尚不清楚，尤其在轨道尺度上的变化机制。本文研究了菲律宾海西部站位 MD06-3047 孔记录的 700kyr 以来温跃层的变化。我们的数据表明该区温跃层温度和盐度的变化与地球倾斜度具有密切的联系，温暖偏咸的温跃层水体对应着高倾角，而温度和盐度偏低的温跃层水体则对应着低倾角。地球倾斜度位于高倾角时，温跃层温度和盐度的增加可能与温暖的北太平洋热带水团对流有关。在研究区域，上部水体冰期较低的垂向温度差表明温跃层变深，而在间冰期温度差的增加则表明温跃层变浅。东亚冬季风（EAWM）是导致冰期温跃层加深的主要因素，类拉尼娜的环境条件可能也与次表层水体表暖而产生的温跃层加深有关。冰盖边界条件的变化，如：冰盖厚度的增加等，可能是 WPWP 南北部冰期温跃层加深的触发因素，通过强化 EAWM 和热带信风来影响 WPWP 温跃层的变化。

ABSTRACT: Variations in thermoclinal conditions play an important role in the evolution of the Western Pacific Warm Pool (WPWP) and in connecting the tropical and extratropical regions of the Pacific Ocean. However, secular thermoclinal changes in the northwestern part of the WPWP and their forcing mechanisms are not yet well understood, particularly on orbital timescales. In this study, we report thermoclinal variation at Site MD06-3047 B in the western Philippine Sea over the last 700 kyr. Our data show that variations in thermocline temperature and salinity in the study area were correlated with changes in Earth's obliquity, with warmer and saltier (colder and fresher) thermocline waters corresponding to high (low) Earth-axial obliquity. At high obliquity, increases in thermocline temperature and salinity may have been linked to advection of warm North Pacific tropical water. In the study area, a lower (higher) vertical temperature gradient in the upper water

column suggests a deeper (shallower) thermocline during glacials (interglacials). The main factor leading to thermoclinal deepening during glacials was strengthening of the East Asian winter monsoon (EAWM), and more La Nina-like conditions may have contributed to concurrent subsurface warming and thus thermoclinal deepening. In-phase thermoclinal deepening in the northern and peri-equatorial southern WPWP during glacial stages may have been triggered by changes in glacial boundary conditions, such as increased ice sheet thickness, through intensification of the EAWM and strengthening of the tropical Trade Winds.

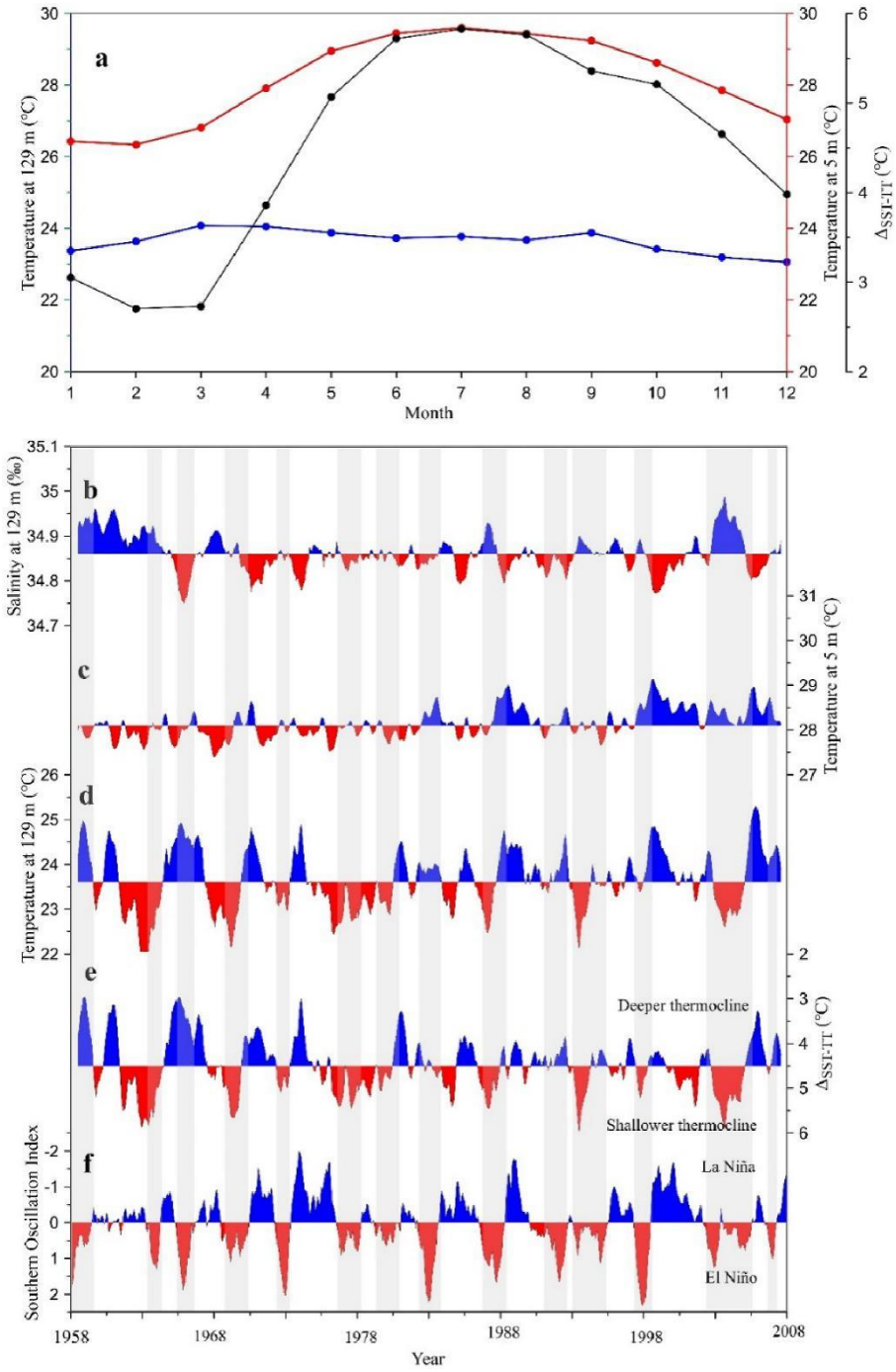

Figure 1. (**a**) Mean monthly SST (at a water depth of 5 m; red line) and mean monthly thermocline temperatures (TT, at a water depth of 129 m, i.e., close to the average calcification depth of *P. obliquiloculata*; blue line), and the difference between the SST and TT records, i.e., $\Delta_{SST\text{-}TT}$ (black line). Data are averaged over the interval from AD 1958–2007. Time series over the interval 1958–2007 for (**b**) thermocline salinity, at a water depth of 129 m; (**c**) SST at a water depth of 5 m; (d) TT, at a water depth of 129 m; (**e**) $\Delta_{SST\text{-}TT}$ near the site of core MD06-3047B; and (**f**) the

Southern Oscillation Index, which is a proxy for ENSO variability. Mean annual SST, TT and $\Delta_{SST\text{-}TT}$ values were calculated over 11 months in order to remove seasonality. Increases (decreases) in $\Delta_{SST\text{-}TT}$ are observed during the summer (winter) as well as during El Niño (La-Niña) events. The ENSO information are from http://ggweather.com/enso/oni.htm. Temperature and salinity data are from Carton-Giese SODA Version 2.0.2–4 (Carton and Giese, 2008, http://iridl.ldeo.columbia.edu/SOURCES/.CARTON-GIESE/SODA/.v2p0p2-4/.ssh/.)

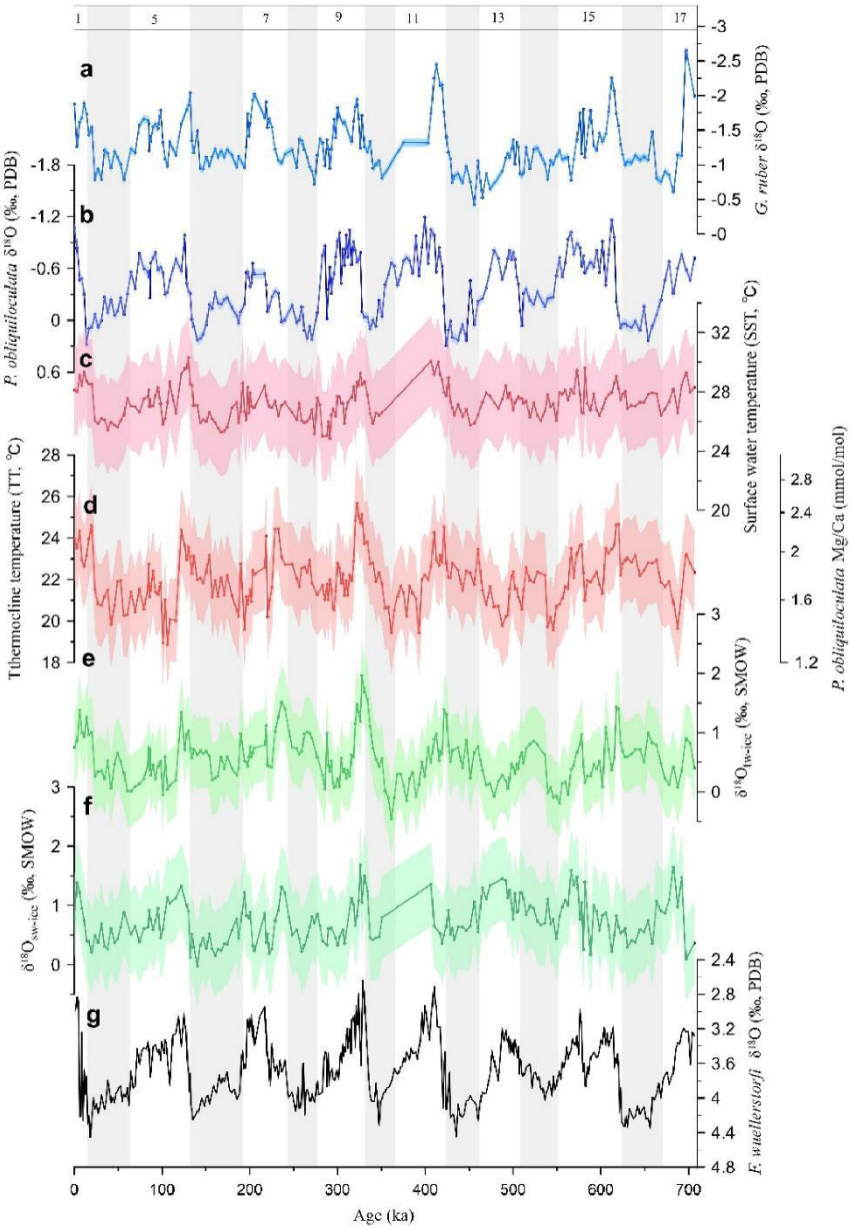

Figure 2. Planktic foraminiferal proxy records of core MD06-3047 B. (**a**) *G. ruber* $\delta^{18}O$ (Jia et al., 2018); (**b**) *P. obliquiloculata* $\delta^{18}O$; (**c**) *G. ruber* Mg/Ca-based SST (Jia et al., 2018); (**d**) *P. obliquiloculata* Mg/Ca-based TT; (**e**) $\delta^{18}O_{tw-ice}$ (calculated based on the temperature-$\delta^{18}O_{calcite}$

equation of Bemis et al., 1998; the component of $\delta^{18}O_{tw-ice}$ attributable to changes in local/regional hydrology was then calculated by subtracting the influence of continental ice volume taken from Bintanja et al., 2005); (**f**) $\delta^{18}O_{sw-ice}$ of core MD06-3047 B; and (**g**) *F. wuellerstorfi* $\delta^{18}O$ (Jia et al., 2018; note that this record was used to establish an age model for core MD06-3047 B. Gray vertical shading indicates even-numbered MIS; colored shading for individual records represents error ranges.

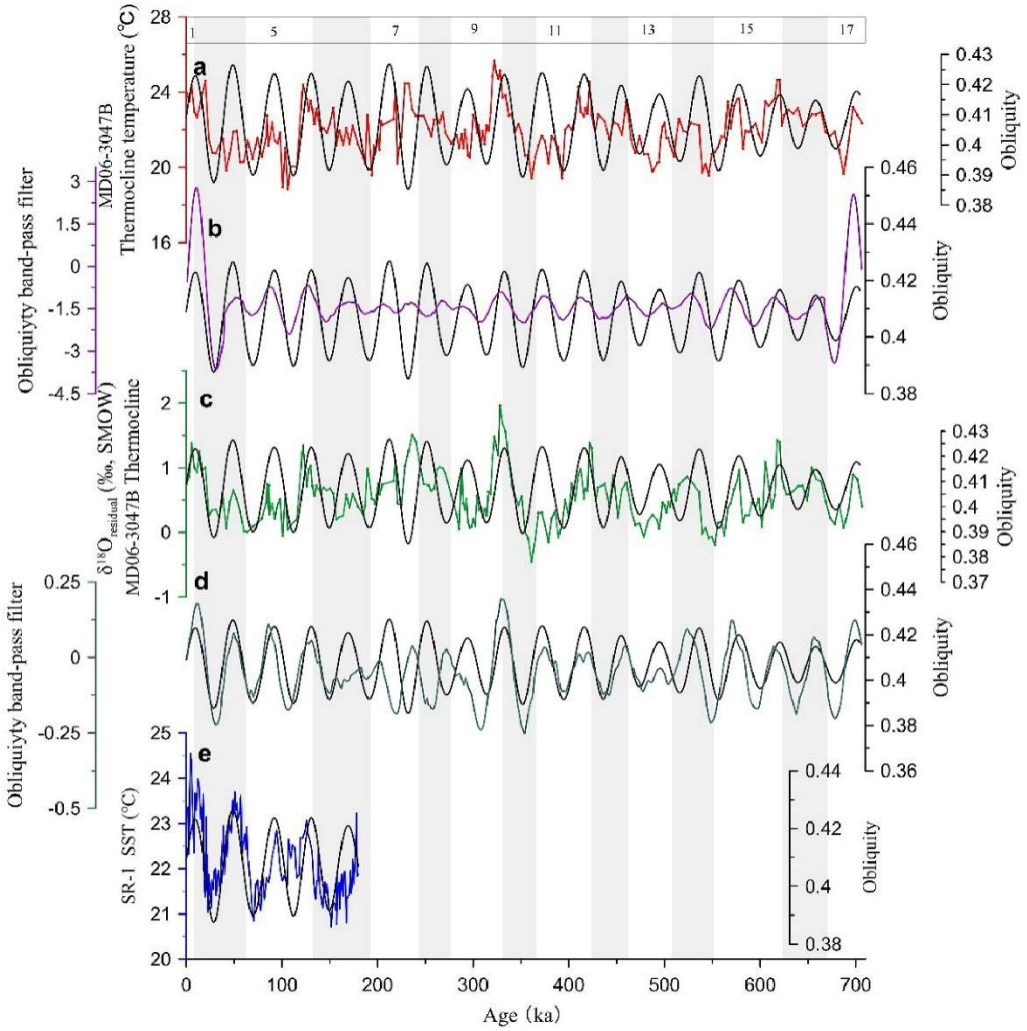

Figure 3. Relationship between TT and δ18Otw–ice of core MD06-3047 B and Earth's axial obliquity. (**a**) *P. obliquiloculata* Mg/Ca-based TT; (**b**) comparison of obliquity and the band-pass filtered TT record using a frequency of 0.024 kyr^{-1}; (**c**) $\delta^{18}O_{tw-ice}$ record; (**d**) comparison of obliquity and band-pass filtered $\delta^{18}O_{tw-ice}$ records using a frequency of 0.024 kyr^{-1}; (**e**) comparison with obliquity and SST records of core SR-1 (Itou et al., 2014). The obliquity data are from Laskar

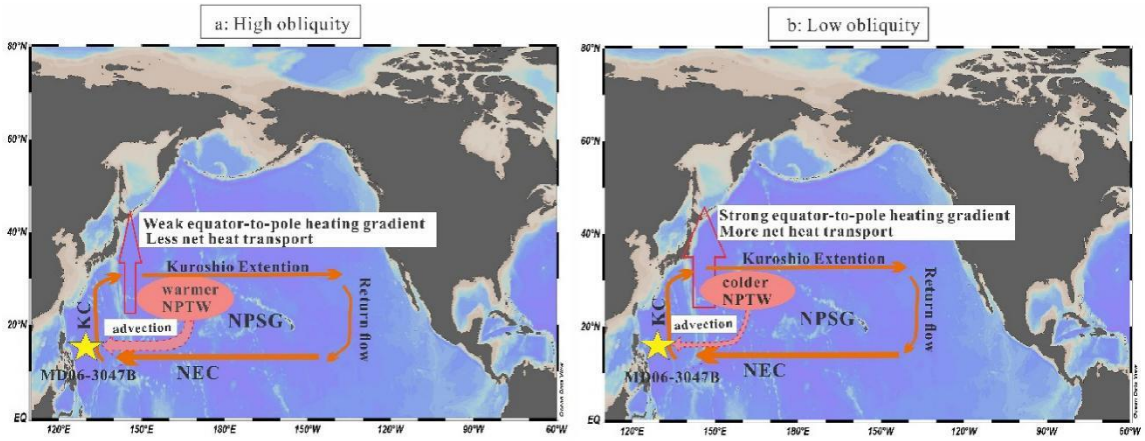

Figure 4. Schematic diagram of variability in net heat transport, North Pacific Subtropical Gyre (NPSG) flow, and formation of NPTW during (**a**) high-obliquity and (**b**) low-obliquity intervals.